

Project	Advies Schadebeoordeling IMG Modelberekeningen schade in gebouwen ten gevolge van diepe bodemdaling
Report number	01
Date	February 19, 2021
Version	05

COMPUTATIONAL MODELLING CHECKS OF MASONRY BUILDING DAMAGE DUE TO DEEP SUBSIDENCE

Client: IMG

Authors Jan G. Rots
 J.G.Rots@tudelft.nl
 Paul Korswagen Eguren
 P.A.KorswagenEguren@tudelft.nl
 Michele Longo
 M.Longo@tudelft.nl

Address Delft University of Technology
 Faculty of Civil Engineering and Geosciences
 Stevinweg 1, 2628 CN, Delft

 Faculty of Civil Engineering and Geosciences Stevinweg 1 2628 CN Delft PO 5048 2600 GA Delft www.citg.tudelft.nl	Report	
	<i>Title:</i>	Computational modelling checks of masonry building damage due to deep subsidence
	<i>Author(s):</i>	Jan G. Rots Paul Korswagen Eguren Michele Longo
	<i>Date:</i>	February 19, 2021
<i>Client(s):</i> IMG	<i>Version:</i> 05	
<i>Project number:</i>	<i>Project name:</i> Advies Schadebeoordeling IMG Modelberekeningen schade in gebouwen ten gevolge van diepe bodemdaling	<i>File reference:</i>
<i>Cite as:</i> Rots, J.G., Korswagen, P.A., Longo, M. (2021). Computational modelling checks of masonry building damage due to deep subsidence. Delft University of Technology. Report number 01, Version 05, February 19, 2021.		

Copyright statement

All rights reserved. No part of this publication may be reproduced, stored in a retrieval system of any nature, or transmitted, in any form or by any means, electronic, mechanical, photocopying, recording or otherwise, without the prior written permission of TU Delft.

Liability statement

TU Delft and those who have contributed to this publication did exercise the greatest care in putting together this publication. However, the possibility should not be excluded that it contains errors and imperfections. Any use of this publication and data from it is entirely on the own responsibility of the user. For everybody who has contributed to this publication, TU Delft disclaims any liability for damage that could result from the use of this publication and data from it, unless the damage results from malice or gross negligence on the part of TU Delft and/or those who have contributed to this publication.

Management Samenvatting

IMG heeft TNO en TU Delft gevraagd advies uit te brengen over criteria ter beoordeling van schade ten gevolge van diepe bodemdaling en –stijging bij de gasopslag Norg en diepe bodemdaling bij het Groningenveld. Componenten onder het advies zijn (1) een analytische studie naar de mate van verticale en horizontale bodemvervorming aan het maaiveld, (2) een InSAR analyse van waarnemingen van verticale bodemvervorming aan het maaiveld, (3) een literatuurstudie naar bestaande kennis over de respons van metselwerkgebouwen op bodemvervorming, en (4) deze modelstudie naar de respons en schade van metselwerkgebouwen ten gevolge van diepe bodemdaling. De verwachting is dat de opgetreden of nog op te treden maaiveldvervormingen ten gevolge van de directe effecten van diepe bodemdaling bij gasopslag Norg en het Groningenveld onder grenswaarden liggen waarbij schade zou kunnen optreden. De beschikbare kennis uit literatuur, bijv. [6], hoofdstuk 12.4 uit [16], en [12], gaat uit van empirische modellen die een gebouw als een eenvoudige equivalente ligger schematiseren, in combinatie met een impliciet rek-criterium voor schade. Hoewel breed toegepast, kunnen nog steeds vragen bij deze methode worden geplaatst, bijvoorbeeld ten aanzien van de bepaling van rekken in het metselwerk en de objectiviteit van het begrip “kritische rek” als schademaat.

Om extra zekerheid in te bouwen is door TU Delft een aanvullende modelstudie uitgevoerd naar de invloed van diepe bodemdaling op bovenliggende metselwerkgebouwen. Deze modelstudie is uitgevoerd op basis van de eindige-elementenmethode. Hierbij is een expliciet schade-criterium gehanteerd (de ‘Psi’-benadering [7,8,9] die rechtstreeks scheurwijdte, scheurlengte en scheuraantal in zich bergt en daarmee kan discrimineren binnen de laagste schadeklasse) in combinatie met conservatieve, worse-case model-aannames. Dit rapport doet verslag.

De aanpak is drie-laags. De modellering begint met een groot model (laag 1) waarin een denkbeeldige gasopslag op diepte wordt leeg getrokken (extractie) of opgepompt (injectie). De vervormingen van dit grote model worden doorgegeven aan een kleiner model (laag 2) nabij de oppervlakte, en vervolgens aan een detailmodel (laag 3) van een metselwerkgevel. Het laag-1 model blijkt krommingen en horizontale rekken aan het maaiveld goed te kunnen representeren. Het laag-1 model is gekalibreerd en aangepast aan analytische geo-mechanische studies van TNO voor het jaar 1995 dat de maximaal opgetreden daling bij gasopslag Norg represeneert [13], welke op hun beurt vergeleken zijn met InSAR satellietaanvullingen en GPS-data voor de periode 2015-2019 [10]. Het resultaat van dit laag-1 model is vervolgens via laag 2 bruikbaar in gekoppelde, semi-gekoppelde of ontkoppelde berekeningen [1,6] van de gevel (laag 3).

De aansname van ontkoppelde berekeningen is de meest ongunstige, ofwel conservatief. Hierbij wordt verondersteld dat alle grondvervorming (zowel verticaal als horizontaal) volledig wordt doorgegeven aan het gebouw. In werkelijkheid heeft het gebouw stijfheid en massa en zal daardoor aanmerkelijk minder vervormen dan de grond ter plaatse van het maaiveld. Naast dit meest ongunstige scenario zijn variatiestudies uitgevoerd waarbij niet 100% maar resp. 75, 50, 25 en 0% van de horizontale grondvervorming wordt overgedragen op het gebouw terwijl in alle gevallen de verticale grondvervorming wordt doorgegeven. Uit literatuur is bekend dat slechts een klein percentage horizontale overdracht reëel is, indicatie 30% [5].

Verder is de locatie van het gebouw op de meest ongunstigste denkbare plek in de dalingskom aangenomen, ter plaatse van de grootste kromming en horizontale rek, zowel voor neerbuiging (sagging, bij gas-extractie) als opbuiging (hogging, bij gas-injectie).

Drie verschillende gevels zijn onderzocht, een lange gevel met kleine openingen, een lange gevel met grote openingen en een korte gevel met openingen. Bij alle gevallen is eerst de daadwerkelijke bodemvervorming opgelegd, waarbij in geen der gevallen scheurvorming werd geconstateerd. Vervolgens is telkens de bodemvervorming proportioneel opgeschaald totdat zichtbare schade optrad. Zichtbare schade komt overeen met een scheur met een breedte van 0.1 mm en een lengte van minimaal 100 mm, conform genoemde ‘Psi’-methodiek. De factor van opschaling represeneert de marge (reserve) tot het ontstaan van zichtbare scheurvorming.

Het resultaat is dat de marge (reserve) tot het ontstaan van een eerste zichtbare scheur varieert van een factor 5,5 tot 110 voor de onderzochte casussen. De factor 5,5 correspondeert met het meest ongunstige geval: 100% overdracht van de horizontale rekken, voor hogging, de lange gevel met kleine openingen, gepositioneerd op de meest ongunstige plek in de dalingskom resp. de stijgingskom. Voor de casussen met 25% horizontale overdracht (vergelijkbaar met de realistische 30% genoemd in [5]) bedraagt de marge een factor 16 tot 39.

In bijlagen zijn vijf aspecten nader uitgediept:

- De invloed van de grond-gebouw interface.

Als variatie op de volledig ontkoppelde analyses, is een controlestudie uitgevoerd naar de mogelijke invloed van het meenemen van wrijvingsslip en gaping tussen gebouw en grond. Voor sagging blijkt de invloed gering. Voor hogging blijkt de marge/reserve tot het moment van zichtbare schade nog verder toe te nemen.

- De invloed van de cyclische belasting bij het jaarlijks onttrekken en injecteren van gas.

Als variatie op bovenstaande monotone analyses zijn twee cyclische belastingprotocollen doorgerekend, met tien jaarcycli, in resp. een -1 down en +0.5 up scenario en een +1 up en -2 down scenario voor sagging en hogging. Bij ongeschaalde daadwerkelijke bodemvervormingen volgens [13] heeft het cyclische effect geen invloed, omdat het metselwerk in alle gevallen elastisch blijft (niet scheurt). Pas wanneer de bodemvervormingen in de eerste cyclus ver worden opgeschaald totdat zichtbare scheurvorming ontstaat (d.w.z. marges opvoeren van 5.5 en hoger, afhankelijk van de casus) blijkt het cyclische effect tot een toename van schade te leiden (een 'delta Psi'). Er kan worden geconcludeerd dat het cyclische effect van de seizoenvariatie van gasonttrekking en gasinjectie pas tot een toename van zichtbare schade kan leiden als de verplaatsingen en rekken ten gevolge van de diepe bodemdaling aanmerkelijk groter zijn dan waargenomen in de afgelopen decennia.

- De invloed van metselwerkeigenschappen.

Gevoeligheidsstudies zijn uitgevoerd naar de invloed van metselwerkeigenschappen voor baksteen en cellenbeton, door zwakkere varianten door te rekenen. De marge/reserve tot zichtbare scheurvorming varieert dan van -33% tot +67% ten opzichte van eerder genoemde marges voor metselwerk met gemiddelde eigenschappen, afhankelijk van de casus, met 100% overdracht. De marges zijn nog steeds groot, ook gezien de worst-case benadering op andere aspecten (meest ongunstige positie van de gevels, 100% overdracht).

- De invloed van het funderingstype.

Naast de traditionele metselwerkfundering zijn andere ondiepe funderingen onderzocht. Modernere betonnen funderingen produceren allemaal marges/reserves die gelijk of hoger zijn dan die van de metselwerkfundering, voor een 100% overdracht van de horizontale rekken. Wanneer een niet-lineaire grond-gebouw interface wordt opgenomen, nemen de marges aanzienlijk toe; dit suggereert dat zelfs muren van zeer slecht metselwerk of andere kwetsbare materialen niet zouden worden aangetast als ze op betonnen funderingen worden gebouwd.

- De invloed van voor-schade

De invloed van bestaande schade is meegenomen door op ongunstige plekken in de gevels vooraf scheuren aan te brengen. Deze scheuren verminderden de marge met maximaal een factor 2; toch is de laagste marge/reserve nog steeds een factor van ongeveer 2.8 bij de ongunstigste aanname van 100% horizontale overdracht, en een factor 8.8 bij de aanname van 25% horizontale overdracht, waarbij ook een geval in combinatie met cyclische belasting is beschouwd

Op basis van de resultaten van deze modelstudie wordt geconcludeerd dat directe diepe bodemdaling bij gasopslag Norg geen zichtbare schade in het metselwerk geeft. Als de horizontale en verticale bodemvervormingen bij het Groningenveld qua grootte vergelijkbaar zijn met de cyclische bodemvervormingen bij de gasopslag Norg, kan deze conclusie worden doorgetrokken naar het Groningenveld.

Table of Contents

MANAGEMENT SAMENVATTING	3
1. INTRODUCTION	6
2. FEM SOIL MODEL	7
2.1 DEEP-SOIL MODEL.....	7
2.2 SHALLOW-SOIL MODEL	10
2.3 CONCLUSIONS.....	12
3. FEM NON-LINEAR FAÇADE MODEL	13
3.1 FAÇADES A AND B.....	13
3.2 FAÇADE C.....	18
3.3 SENSITIVITY STUDY – REDUCED STRAIN TRANSFER.....	22
3.4 SUMMARY OF RESULTS	23
4. DISCUSSION AND CONCLUSIONS	26
5. REFERENCES	28
APPENDIX A: MATERIAL PARAMETERS.....	29
A.1 SOIL.....	29
A.2 MASONRY	30
APPENDIX B: SENSITIVITY STUDY – SOIL-STRUCTURE INTERFACE	31
B.1 INTRODUCTION	31
B.2 METHOD.....	31
B.3 RESULTS.....	32
B.4 CONCLUSIONS	36
APPENDIX C: SENSITIVITY STUDY – CYCLIC LOADING	37
C.1 INTRODUCTION	37
C.2 METHOD.....	37
C.3 RESULTS.....	38
C.4 CONCLUSIONS	41
APPENDIX D: SENSITIVITY STUDY – MASONRY MATERIAL PROPERTIES	42
D.1 INTRODUCTION AND METHOD	42
D.2 RESULTS.....	43
D.3 CONCLUSIONS.....	44
APPENDIX E: SENSITIVITY STUDY – FOUNDATION	45
E.1 INTRODUCTION.....	45
E.2 METHOD	46
E.3 RESULTS.....	46
E.4 CONCLUSIONS	48
APPENDIX F: SENSITIVITY STUDY – PRE-DAMAGE.....	49
F.1 INTRODUCTION.....	49
F.2 METHOD	49
F.3 RESULTS	51
F.4 CONCLUSIONS	53

1. Introduction

In recent years, gas extraction and gas storage in the Groningen region is leading to deep subsidence and earthquakes which may cause aesthetical and structural damage to masonry buildings.

This report describes computational modelling checks as to whether the direct effect of deep subsidence may cause damage to masonry facades. The focus is on the case of the gas extraction/injection storage at Norg. The extraction/injection leads to vertical and horizontal displacement profiles of the soil at greenfield level (soil surface). The strategy is to apply these soil movements, available from analytical geomechanics models and satellite and GPS based field data, to different masonry facades and study the initiation and propagation of cracks in the masonry. The finite element method will be used in a three-tiered approach, starting from a deep soil model, via a shallow soil model up to a detailed façade model. In this process, worse case assumptions will be employed, so that the results provide insight into the margins with respect to the onset of visible damage. The computational results then serve to underpin analytical lower bound criteria from literature and from companion work packages of this IMG project on building damage due to deep subsidence.

2. FEM Soil Model

2.1 Deep-Soil Model

2.1.1 Description

For the modelling, a 3-tiered approach is employed. The settlement profile produced by the extraction/injection (shrinkage/expansion) of the gas storage in the underground soil is simulated via a soil model that includes the location where this process takes place. Thus, a soil block of 8x3 km (named Deep Soil Model) is numerically modelled by the software DIANA FEA 10.4 [1]. The soil model is represented in 2D in plane strain condition (i.e. studying a representative critical cross-section of the actual 3D situation and settlement trough) and it is divided into different horizontal layers over the height. Material properties and thickness of the soil layers are specified in Appendix A. Figure 1 depicts an overview of the geometry of the Deep Soil Model, while its finite element mesh is shown in Figure 2. The model is subjected to gravity load (after initializing the soil stress condition) and subsequently to a prescribed shrinkage strain applied to an area of 250x200 m located at the centre of the bottom edge of the model. The strain is applied in both horizontal (X) and vertical (Y) direction with an amplitude of 0.5%. Both shrinkage and expansion situations are analysed, aiming to simulate both extraction from and injection to a gas storage. These cases will provide sagging (settlement and downward curvature at the surface) and hogging (heave and upward curvature at the surface) respectively.

Quadratic 8-noded plane strain elements (CQ16E and CT12E) are used to model the soil. The model is restrained vertically at the base and horizontally at the two sides. The mesh dimensions range from 50x50 m at the bottom to 5x5 m at the top.

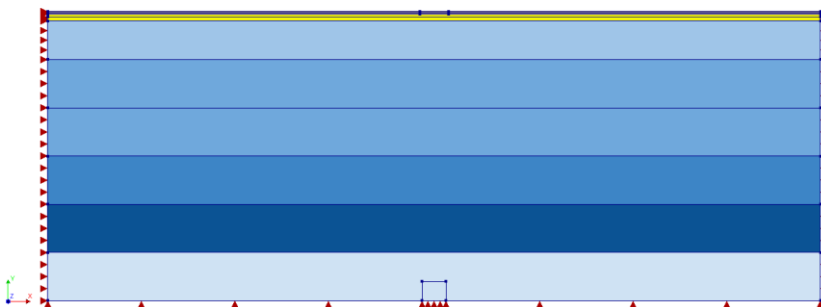


Figure 1. Geometry and boundary conditions of layered Deep Soil Model.

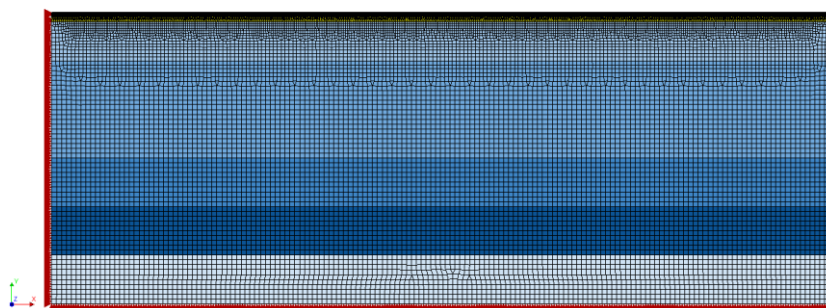


Figure 2. Finite element mesh for Deep Soil Model.

2.1.2 Results

Contour plots of displacements and horizontal strains generated by the Deep Soil Model are depicted in Figure 3, Figure 4 and Figure 5. Results at the surface of the model are plotted in Figure 6. Comparing Figures 6 and 7, the vertical displacements of the Deep Soil Model show a good agreement with the vertical displacements from the analytical model in [12], both regarding the shape of the profile and the amplitude. The horizontal displacement profiles and the derived horizontal strains from the Deep Soil Model again show a good comparison with the analytical model when it comes to the shape of the profile, but now the amplitude is overestimated compared to the analytical results. In order to evaluate the effects of the soil movements to a set of façades, the vertical displacements of the Deep Soil Model are used directly but the amplitude of the horizontal displacements (and strains) of the Deep Soil model has been scaled to that of the analytical model from [13] for this location of Norg. This is because 1) the Deep Soil model is a simplification in 2D while the analytical model also considers the 3D effects; 2) the Deep Soil model assumes the effect of the gas with shrinking and expanding elements which is a crude approximation of reality; 3) the applied strain is uniform over a certain assumed area which in reality could have a different size and different strain distribution; 4) close to the gasfield, localised non-linear effects could play a role which are not modelled in the linear-elastic soil model. Consequently, while the shape of the deformation has been maintained, its magnitude has been scaled to that of the more reliable geomechanical analytical model. The scaled results of displacements and strains are shown in Figure 8.

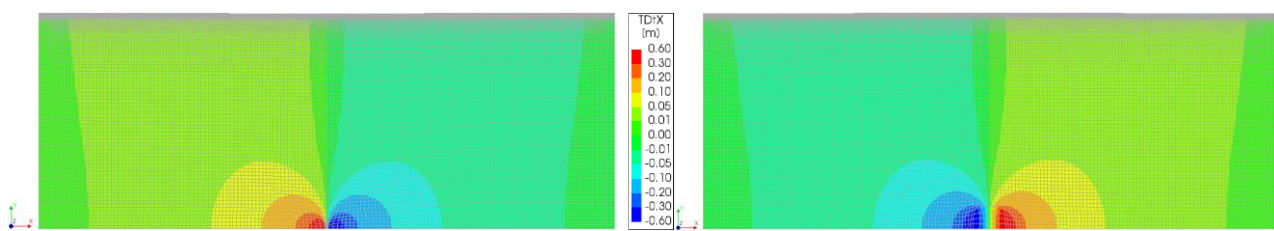


Figure 3. Horizontal displacement Deep Soil Model subjected to shrinkage (gas extraction, left) and expansion (gas injection, right). Deformed mesh magnified x200.

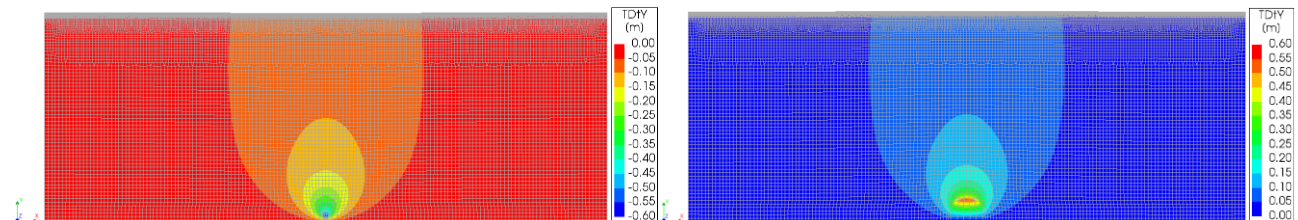


Figure 4. Vertical displacement Deep Soil Model subjected to shrinkage (gas extraction, left) and expansion (gas injection, right). Deformed mesh magnified x200.

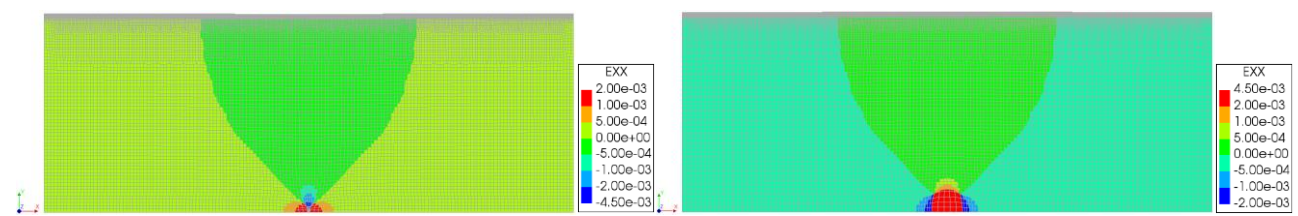


Figure 5. Horizontal strain Deep Soil Model subjected to shrinkage (gas extraction, left) and expansion (gas injection, right). Deformed mesh magnified x200.

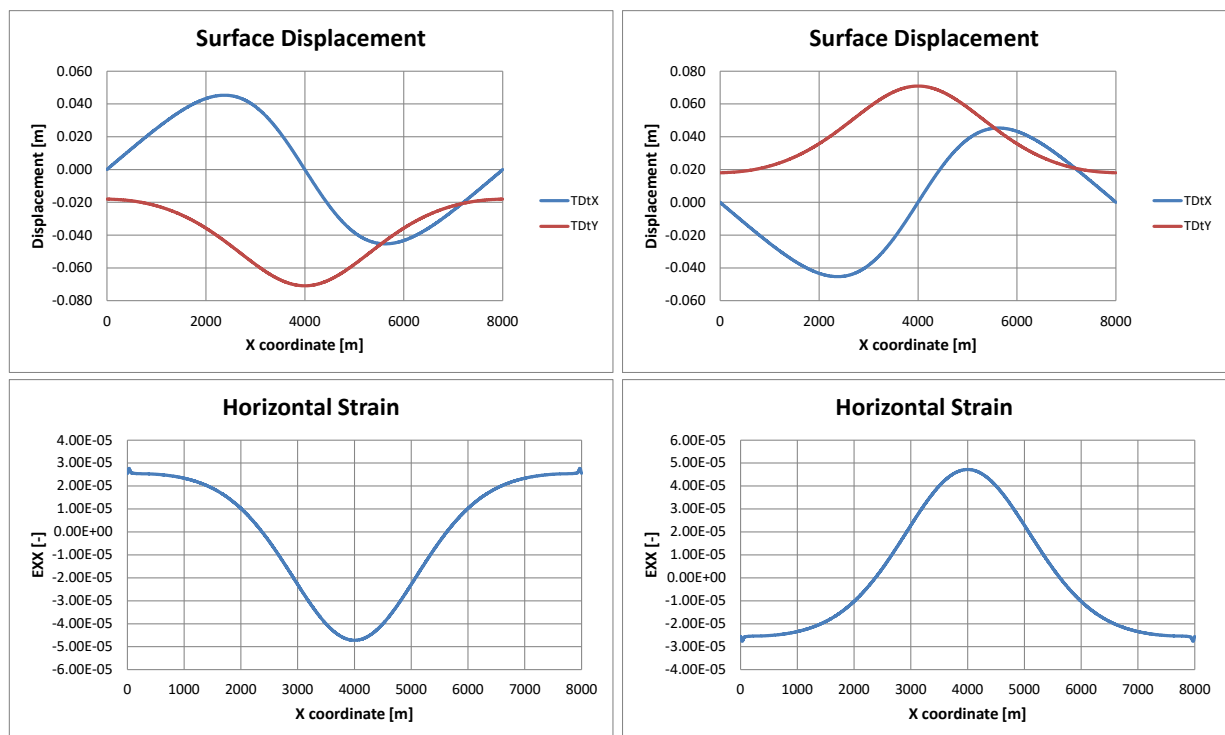


Figure 6. Vertical and horizontal displacements and horizontal strains at surface of Deep Soil Model subjected to shrinkage (left) and expansion (right).

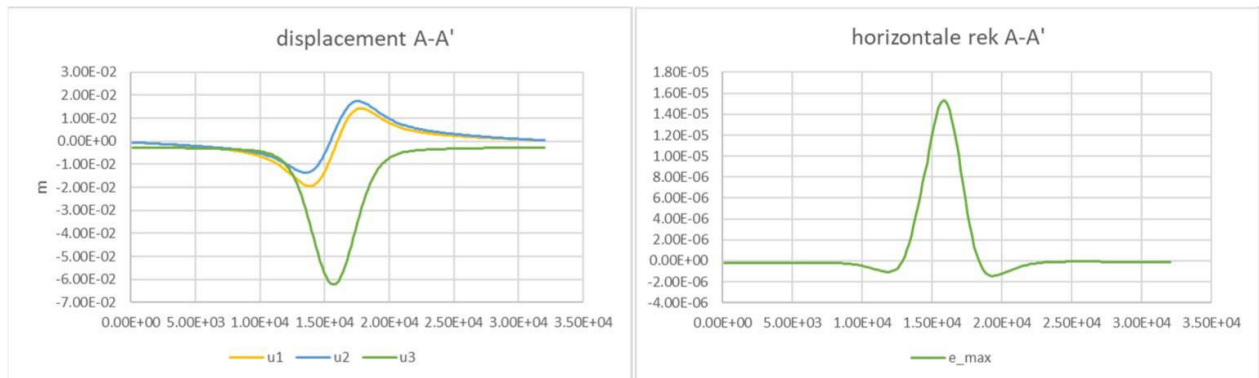


Figure 7. Vertical and horizontal displacements and horizontal strains obtained from analytical geo-mechanics calculations at critical cross-section for the location of Norg Error! Reference source not found..

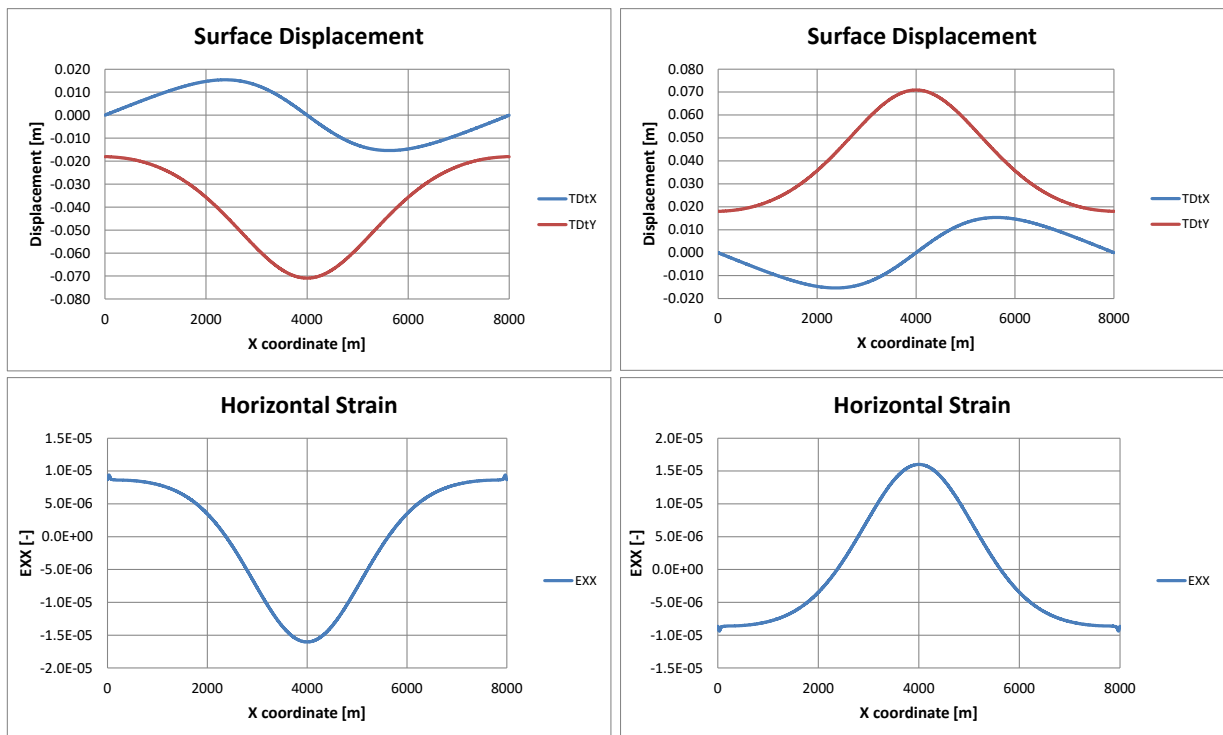


Figure 8. Vertical and horizontal displacements and horizontal strains at surface of Deep Soil Model scaled to the analytical solution amplitude. Shrinkage (left) and expansion (right).

2.2 Shallow-Soil Model

2.2.1 Description

Since the mesh of the Deep Soil Model is too coarse to be able to represent and apply directly the surface displacements to the bottom of a façade, they are “filtered” through a smaller soil block with a finer mesh. This Shallow Soil Model is a portion of the Deep Soil Model, specifically the portion at the surface located in the middle of the model since this is the location with the highest strains and at the same time the highest curvatures. It has a dimension of 300x30 m. The displacements at this location (Figure 9), are extracted and extrapolated from the Deep Soil Model and directly transferred to the Shallow Soil Model. The area in the middle of the model is selected for the subsequent façade analyses. This location can be considered as the worst-case position (Figure 10), as both the curvatures and the horizontal strains display a maximum in that middle. The displacements at this location are thus included as input in the smaller soil model. The Shallow Soil Model has a finer mesh (1x1 m) in order to better capture the displacement at the surface and transfer it later to the facade. An overview of the Shallow Soil Model and its mesh are shown in Figure 11 and Figure 12.

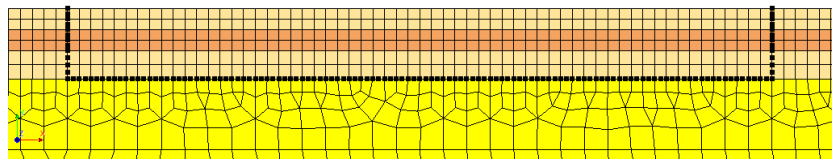


Figure 9. Location of output points in the Deep model used as input in the Shallow model.

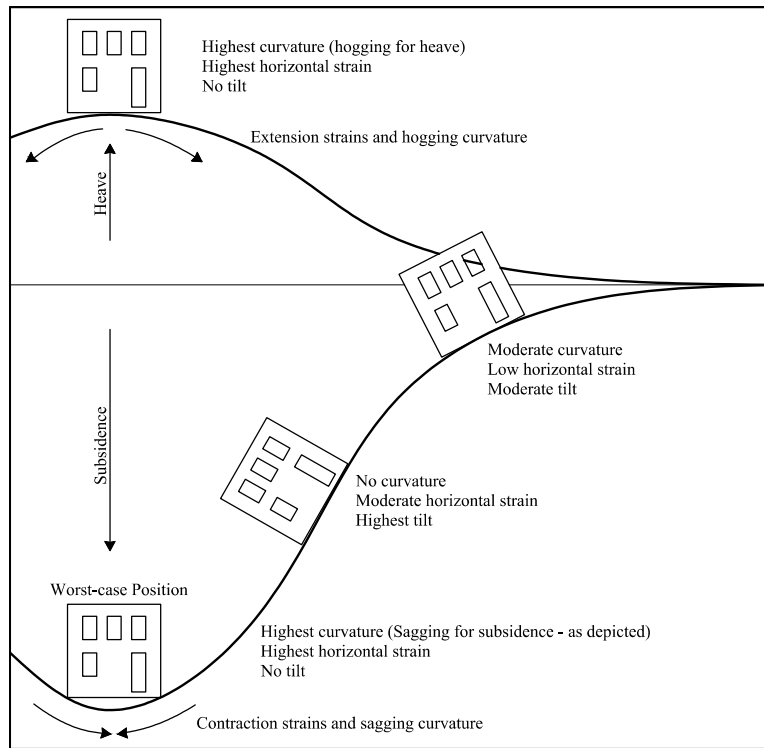


Figure 10. Comparison of a building placed at different locations in the subsidence trough. The sketch is extremely amplified.

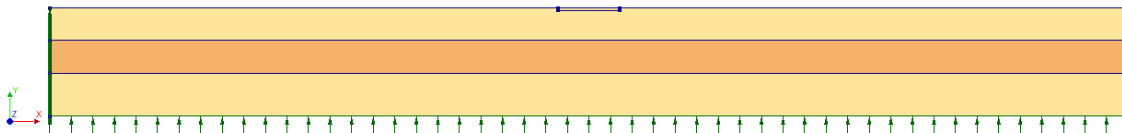


Figure 11. Geometry of Shallow Soil Model.

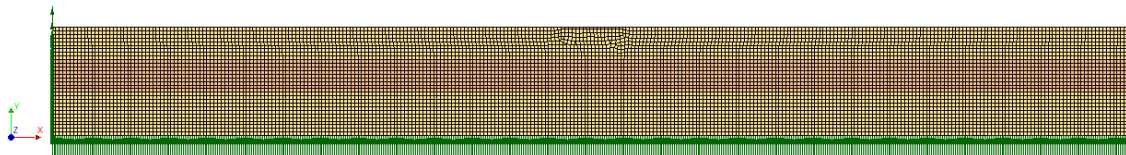


Figure 12. Finite element mesh of Shallow Soil Model.

2.2.2 Results

In a similar fashion as done between Deep and Shallow model, the displacements at the foundation in the Shallow model (Figure 13) are directly assigned as input in the plane stress façade models. The input for the façade models is plotted in Figure 14. Please note that now the length of the horizontal axis is much smaller, complying with the length ranges of the facades selected for study. Therefore, the relative vertical displacement is much smaller than for the long ranges in the previous Figures, while the horizontal displacement profiles appear as being linear over this short range and the horizontal strains as being constant. For sagging, the horizontal displacements move inward towards to centre of the façade (compressive strains), while for hogging the horizontal displacements move outward from the centre of the façade (tensile strains).

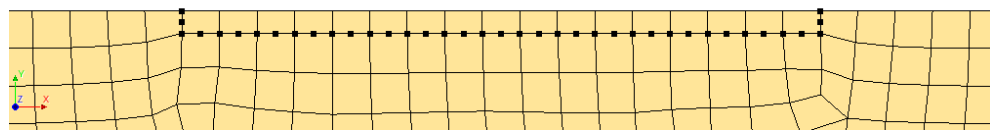


Figure 13. Location of output points in the Shallow model used as input in the Façade model.

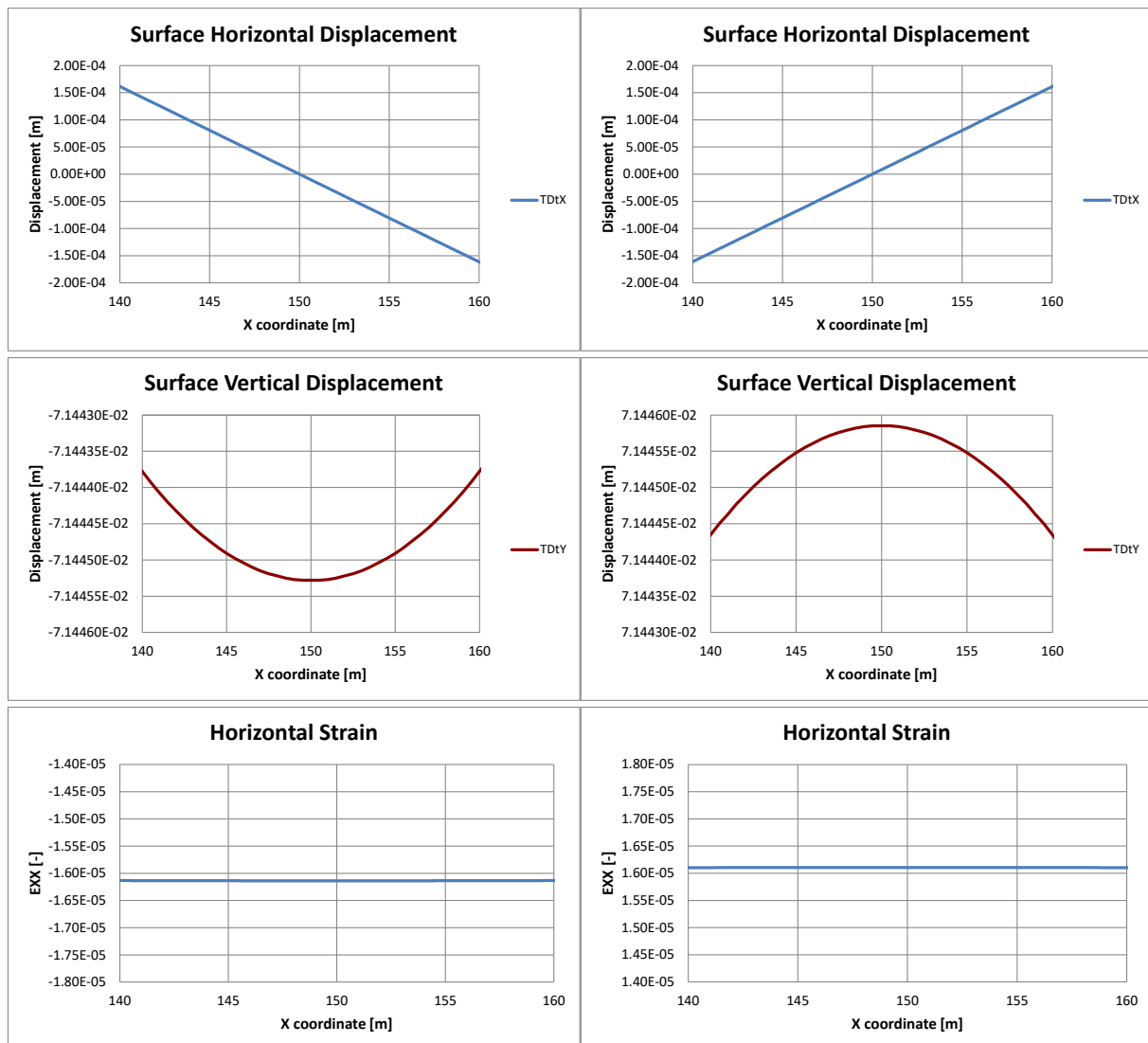


Figure 14. Horizontal, vertical displacement and horizontal strain of surface of Shallow Soil Model. Shrinkage (left) and expansion (right).

2.3 Conclusions

The deep and shallow soil models have been used to estimate the shape of the displacements present at the bottom of the foundation of a façade. For façade hogging due to heave caused by the storage of gas, the horizontal strain appears constant over the length of the foundation and corresponds to an extension of 1.61E-5 m/m (or 16 $\mu\text{m}/\text{m}$) and, over a façade length of 20 metres, the curvature of the soil (a maximum of 3E-8 rad/m) produces a relative vertical displacement of 1.5 μm which corresponds to an angular distortion of 3E-7 rad. For façade sagging due to subsidence caused by the extraction of gas, the horizontal strain is in contraction with the same magnitude of 16 $\mu\text{m}/\text{m}$ and identical inverted curvature.

Ultimately, the magnitude of these strains is not entirely relevant since the following models will determine the margin between these values and those required to initiate visible damage thus leading to critical values for building damage. In this sense, the relationship between horizontal and vertical displacements as established in Figure 14 is more important.

3. FEM Non-Linear Façade Model

The output taken from the Shallow Soil Model is directly applied as prescribed displacement at the foundation of the façade model. This follows the assumption that the horizontal strain from the soil is fully transmitted to the foundation of the masonry façade. It complies with a so-called fully uncoupled situation where the presence of a façade does not affect the deformations in the soil and thus results in a direct transmittal of all ground movements to the structure. In reality, the façade has a stiffness and mass and will therefore interact with the soil (coupling) and consequently reduce the soil deformations; it will flatten the vertical soil displacements and reduce the horizontal soil strains as compared to the free greenfield situation without façade. Consequently, the façade will then undergo a smaller curvature and less horizontal strain; in other words, such 100% transmittal is a conservative, worst-case approach.

The horizontal displacement is applied with an amplitude of 0.14 mm at the sides of the façade, according to Figure 14 top. For the sagging case, positive horizontal displacements are applied to the left side of the façade, while negative horizontal displacements are applied to the right side of the façade (inward movement of the soil to the centre of the façade, at the bottom). For the hogging case, it is the opposite (outward movement of the soil from the centre of the façade). Vertical displacement has a maximum amplitude at the middle of the façade, of about 7.14 mm. Its relative displacement though, between middle and sides of the façade is only about 0.001 mm, thus very small, see Figure 14. The horizontal strain amplitude is about 1.61E-05, almost constant over the length of the façade with a hardly noticeable maximum in the middle of the façade, see Figure 14 bottom.

3.1 Façades A and B

3.1.1 Description

Two façade variations of a farm house are modelled and analysed. Façade A has small openings and façade B has large openings. Both façades are 17 m long and 3.8 m deep on the right side and 2.4 m deep on the left side (representing the shed of a farm house) with a thickness of 210 mm. The foundation, 600 mm deep, is modelled with a thickness of 610 mm. Sensitivity studies on the foundation typology is reported in Appendix E: Sensitivity study – Foundation. Class-III Mindlin beam elements (CL9BE) are placed to the two lateral sides of the façades to simulate the extra stiffness provided by transversal walls. The beam elements have a stiffness equal to 1/3 of the masonry stiffness, with a cross section representing the dimension of a double-wythe wall. This follows the validation of numerical models as in [8] Clay brick masonry properties are assigned to the wall. Overburden due to roof and floor weights are taken into account in the models and assigned as a distributed force. As material model, the Engineering Masonry Model [14, 15] is used. The material properties of the façades are listed in Appendix A. A sensitivity study on the material properties is later performed in Appendix D.

Quadratic 8-noded plane stress elements (CQ16M and CT12M) are used to model foundation and façade. The model is assumed to be fixed base (no soil-structure interaction, i.e. coupling, is considered, the soil displacements are prescribed directly to the bottom of the façade foundation). The mesh is composed of elements with an average size of 200x200 mm. A representation of the models is depicted in Figure 15 and Figure 16.

The façades are subjected to three different types of loads. Gravity load, overburden and displacement due to subsidence are considered in the model. Non-linear calculations are performed. Gravity load is applied first in five equal steps, then overburden is applied in five steps and finally the displacement settlement in twenty load steps. The Secant BFGS (Quasi-Newton) method is adopted as iterative method. Displacement, force and energy norms must be all satisfied during the incremental-iterative procedure within a tolerance of 1% for displacement and force and 0.01% for energy. The Parallel Direct Sparse method is employed to solve the system of equations. The second order effects are considered via the Total Lagrange geometrical nonlinearity.

Shrinkage and expansion of the Deep (and thus Shallow) Soil Model leads to respectively sagging and hogging at the base of the façade, and to a respectively compressive horizontal strain and tensile horizontal strain at the bottom of the façade.

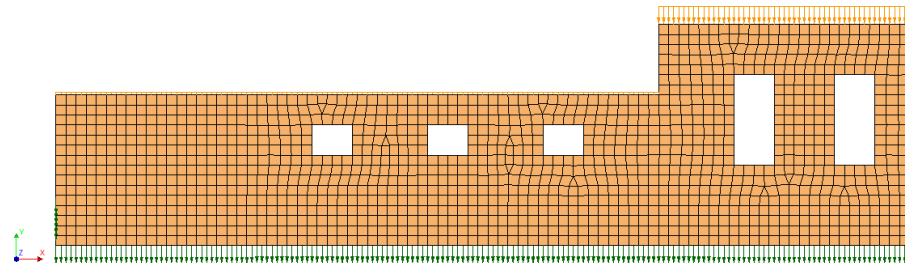


Figure 15. Façade Model A with small openings, finite element mesh.

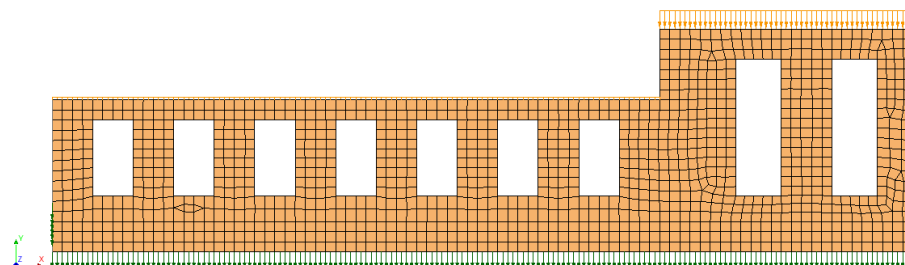


Figure 16. Façade Model B with large openings, finite element mesh.

3.1.2 Original Results

The results for the two different façades when subjected to monotonic sagging and hogging and their corresponding horizontal displacements/strains are presented in the subsequent Figures. The Figures show the contours of horizontal and vertical displacement, horizontal strain, horizontal and vertical stress, principal stress and principal stress trajectories. Results are shown for the façade only, excluding the foundation. Additional sensitivity analyses about the effects of adding a nonlinear friction/gapping interface between soil and foundation, about the effect of cyclic loading from seasonal extraction and injection cycles, and about the effect of material properties are evaluated and described in Appendix C, respectively.

Figure 17 and Figure 18 show the horizontal and vertical displacement of façade A and B when subjected to *sagging* settlement. The negative strain applied at the base (Figure 19) produces the horizontal contraction at the base of the façade. Small positive horizontal stresses (Figure 20) are present at the lateral side and above the window openings at the right side. Small positive vertical stresses are shown at the top and bottom of window openings (Figure 21). Contours of principal stresses are depicted in Figure 22. Principal compressive stress trajectories are shown in Figure 23.

Displacements produced by *hogging* settlement for both façade A and B are depicted in Figure 24. The deformed mesh and horizontal strain plot (Figure 26) clearly shows the expansion at the bottom side of the façades due to positive strain. Contrary to the sagging case, the window-banks and spandrels of the façades are almost entirely subjected to positive horizontal stress, though small, with the highest values at bottom and top of window openings at the right side (Figure 27). Figure 28 depicts vertical stresses, which are mostly negative. Positive values are found above and below window openings and at the bottom left corner of the façades mainly due to a tendency of a delamination mechanism between foundation and facade. Principal stress contour and trajectory plots are shown in Figure 29 and Figure 30.

Note that no damage is found for any of the cases; the stresses remain in all cases, below the assumed masonry tensile strength.

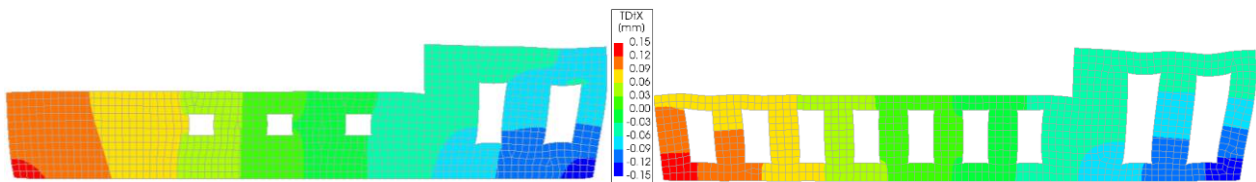


Figure 17. Horizontal displacement façades subjected to *sagging* with axial compressive strain at the base, simulating gas extraction. Façade A (left) and Façade B (right). Deformed mesh magnified x5000.

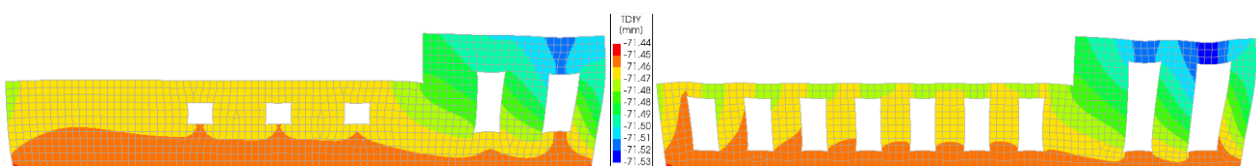


Figure 18. Vertical displacement façades subjected to *sagging*. Façade A (left) and Façade B (right). Deformed mesh magnified x5000.

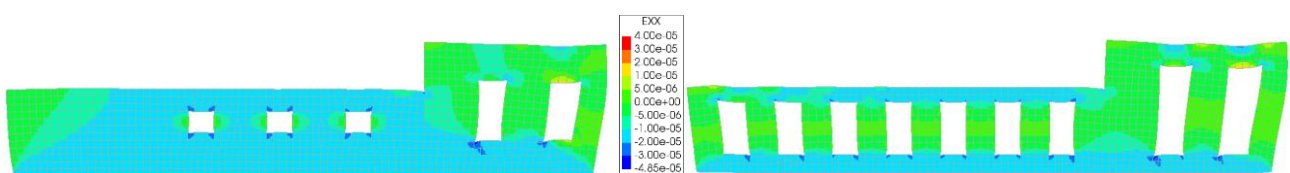


Figure 19. Horizontal strain façades subjected to *sagging*. Façade A (left) and Façade B (right). Deformed mesh magnified x5000.

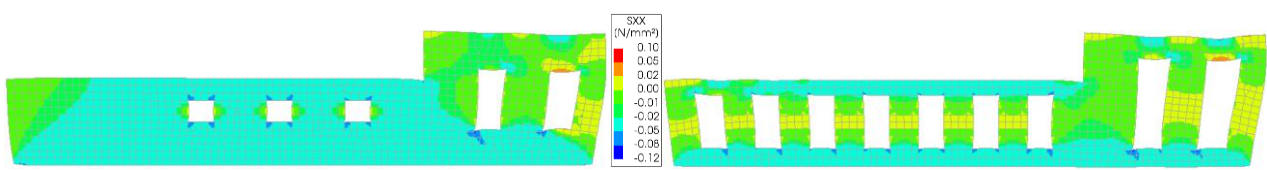


Figure 20. Horizontal stress façades subjected to *sagging*. Façade A (left) and Façade B (right). Deformed mesh magnified x5000.

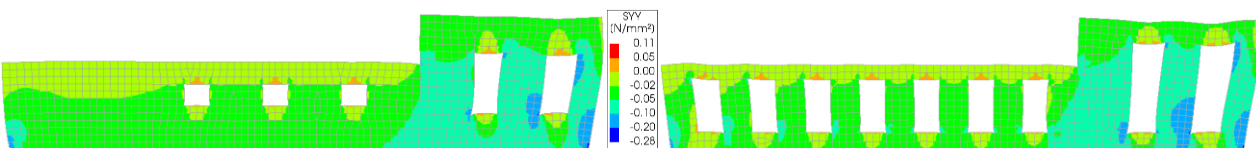


Figure 21. Vertical stress façades subjected to *sagging*. Façade A (left) and Façade B (right). Deformed mesh magnified x5000.

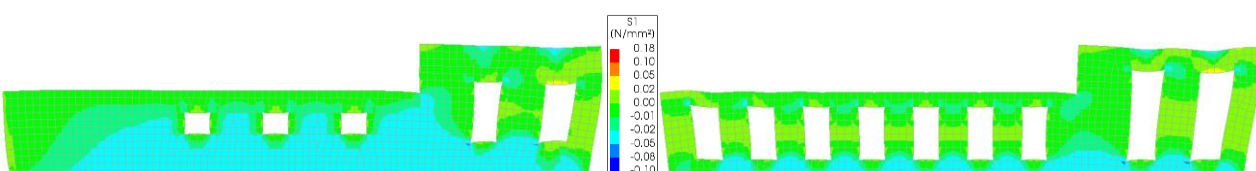


Figure 22. Principal stress façades subjected to *sagging*. Façade A (left) and Façade B (right). Deformed mesh magnified x5000.

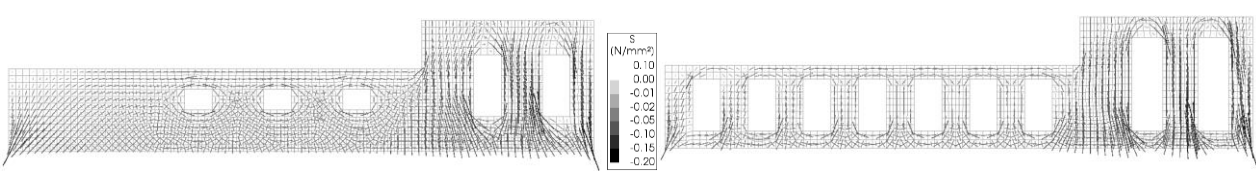


Figure 23. Principal stress compressive tensors façades subjected to *sagging*. Façade A (left) and Façade B (right). No deformed mesh.

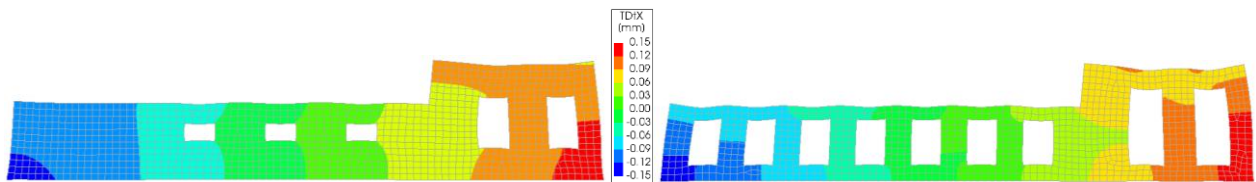


Figure 24. Horizontal displacement façades subjected to *hogging*, with axial tensile strain at the base, simulating gas injection. Façade A (left) and Façade B (right). Deformed mesh magnified x5000.

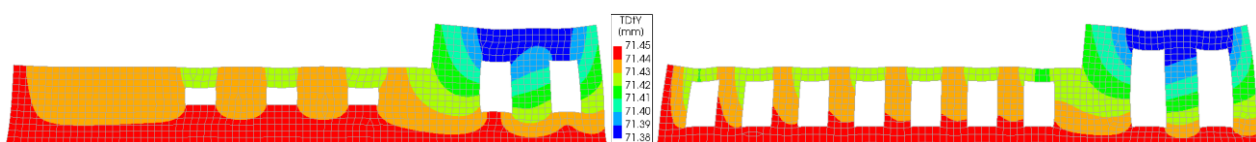


Figure 25. Vertical displacement façades subjected to *hogging*. Façade A (left) and Façade B (right). Deformed mesh magnified x5000.

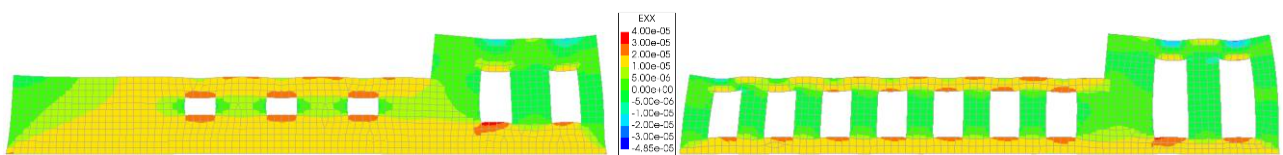


Figure 26. Horizontal strain façades subjected to *hogging*. Façade A (left) and Façade B (right). Deformed mesh magnified x5000.

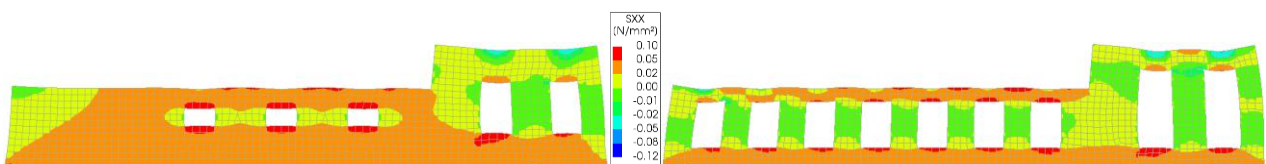


Figure 27. Horizontal stress façades subjected to *hogging*. Façade A (left) and Façade B (right). Deformed mesh magnified x5000.

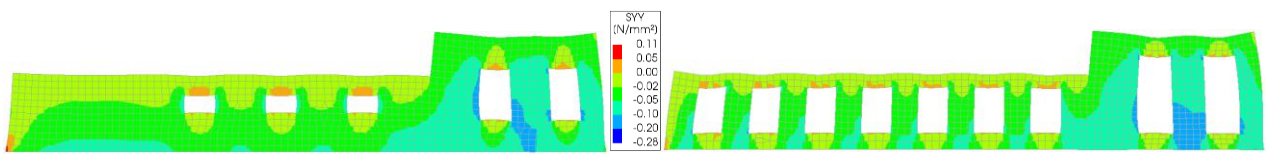


Figure 28. Vertical stress façades subjected to *hogging*. Façade A (left) and Façade B (right). Deformed mesh magnified x5000.

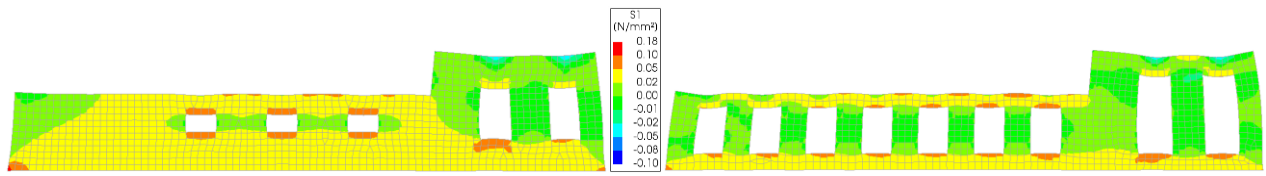


Figure 29. Principal stress façades subjected to *hogging*. Façade A (left) and Façade B (right). Deformed mesh magnified x5000.

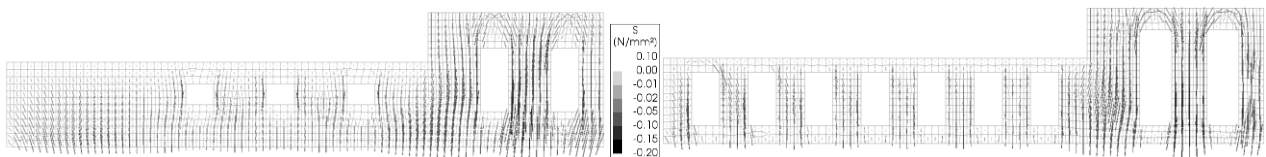


Figure 30. Principal stress compressive tensors façades subjected to *hogging*. Façade A (left) and Façade B (right). No deformed mesh.

3.1.3 Amplified Results

In order to evaluate the onset of visible cracking in the façade, the different displacement cases are iteratively scaled up. The scaling is terminated when the façade reaches the visible damage state. As defined in [7, 9] a façade enters the visible damage state, when a crack, of about 0.1 mm in width and 100 mm in length, is identified. According to [7, 9] this means that the façade has a Psi (scalar damage parameter) equal to 1.0. Please note that the term "visible damage" is herein preferred over "light damage" in order to avoid confusion with different damage scales like the one by Burland et al. summarized in e.g. [6].

Typical crack patterns detected in the two façades when subjected to displacement amplification up to $\Psi_i = 1$, are depicted in Figure 31 and Figure 32. The figures shows the principal crack width for sagging and hogging settlement; for sagging, cracks are mainly localized at the window's corners. For hogging, cracks due to delamination at the two base corners of the façade and cracks below windows openings are present.

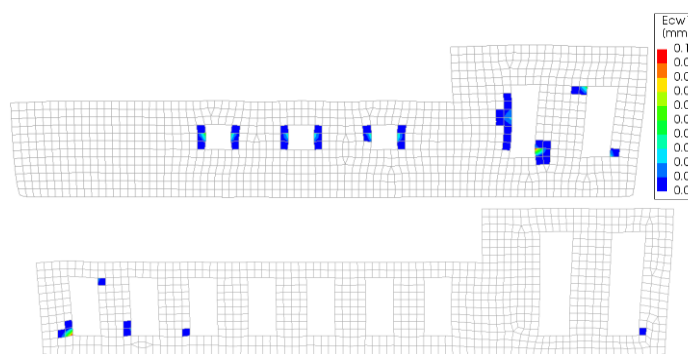


Figure 31. Principal crack width façades subjected to *sagging*. Maximum horizontal displacement applied amplified 11.0 times (about 1.50 mm) for Façade A (left), and 6.25 times (about 0.93 mm) for Façade B (right) in order to reach the visible damage state. Deformed mesh magnified x500.

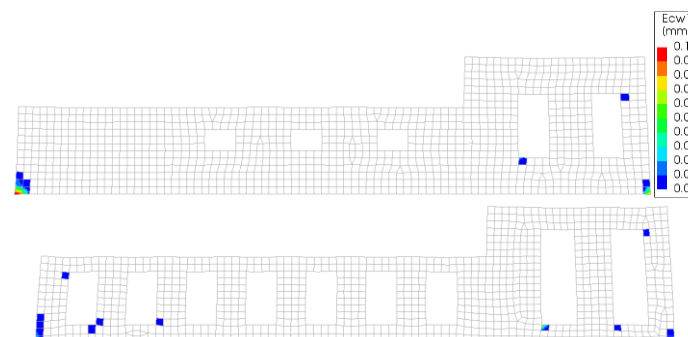


Figure 32. Principal crack width façades subjected to *hogging*. Maximum horizontal displacement applied amplified 5.5 times (about 0.75 mm) for Façade A (left), and 6 times (about 0.82 mm) for Façade B (right) in order to reach the visible damage state. Deformed mesh magnified x500.

3.2 Façade C

3.2.1 Description

In addition to the long facades A and B, a shorter but taller third façade, C, has been modelled. As well as for the previous case, the applied displacement is taken directly from the Shallow Soil Model and scaled to the analytical solution. The prescribed displacements applied at the foundation level are plotted in Figure 14.

The façade with openings is 7 m long and 5.5 m tall with a thickness of 210 mm. The foundation, 600 mm high, is modelled with a thickness of 610 mm. Sensitivity variations on foundation types are performed in Appendix E. Beams are placed to the lateral side as for the previous cases. Clay brick masonry properties are assigned to the wall. As material model, the Engineering Masonry Model is used. The material properties of the façade are listed in Appendix A. For the masonry lintel located above the door, a rotated local axis is considered, so that the bed-joint properties are aligned with the global vertical direction. A sensitivity study on material properties is performed in Appendix D.

Again, quadratic 8-noded plane stress elements (CQ16M and CT12M) are used to model foundation and façade. The model is assumed to be fixed base (no soil-structure interaction, i.e. coupling, is considered, the soil displacements are prescribed directly to the bottom of the façade foundation). The mesh is composed of elements with an average size of 200x200 mm. A representation of the model is depicted in Figure 33.

The façade is subjected to two different type of loads. Gravity load and displacement due to subsidence are considered in the model. A non-linear calculation is performed. Gravity load is applied first in five equal steps, followed by the prescribed displacements in twenty load steps. The same analysis procedure as described in the previous section is employed. Displacement input is directly applied to the foundation and in a monotonic way. A variation study on the boundary conditions is described in Appendix B, where the fixed boundaries are replaced by a set of interface elements. In addition, the effect of a cyclic loading on the façade, is analysed and reported in Appendix C.

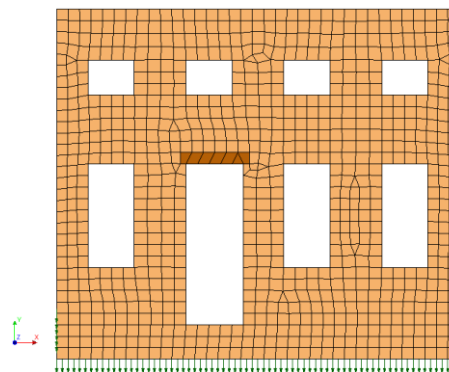


Figure 33. Plane Stress Façade Model C mesh overview.

3.2.2 Original Results

Contour plots of the façade when subjected to *sagging* and *hogging* with their corresponding horizontal displacements/strains are presented. The results show the contours of horizontal and vertical displacement, horizontal strain, horizontal and vertical stress, principal stress and principal stress trajectories. Results are shown for the façade only, excluding the foundation.

Figure 34 and Figure 35 show the horizontal and vertical displacement of façade C when subjected to sagging and hogging. The negative strain applied at the base (Figure 36) produces the horizontal contraction at the base of the façade. Positive horizontal strain and stresses (Figure 36 and Figure 37) are located at the base and at above window openings, mainly at the ground floor for both the sagging and hogging case. Positive horizontal stress are shown for the hogging case at the two base corners, indicate some horizontal

delamination crack between foundation and wall. Lower positive stresses are found in the vertical direction (Figure 38), located mainly at top of window openings. Principal stress contour and tensor of the principal compressive stress are shown in Figure 39 and Figure 40. For all cases no damage is found. The stresses are in all cases below the masonry tensile strength.

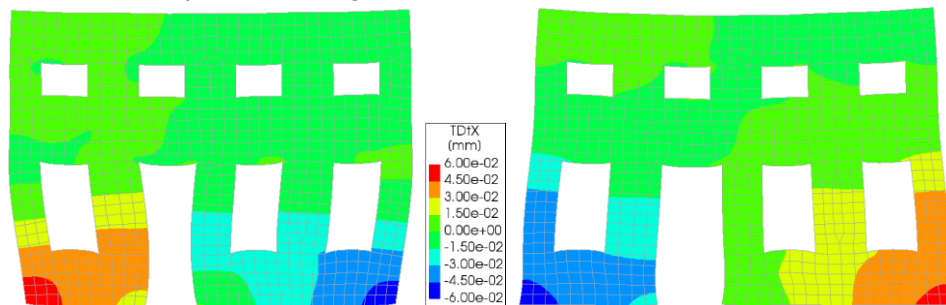


Figure 34. Horizontal displacement façade C when subjected to *sagging* (left) and *hogging* (right). Deformed mesh magnified x5000.

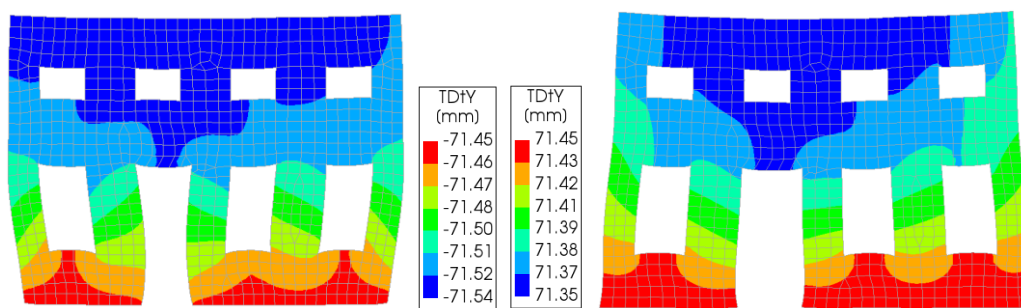


Figure 35. Vertical displacement façade C when subjected to *sagging* (left) and *hogging* (right). Deformed mesh magnified x5000.

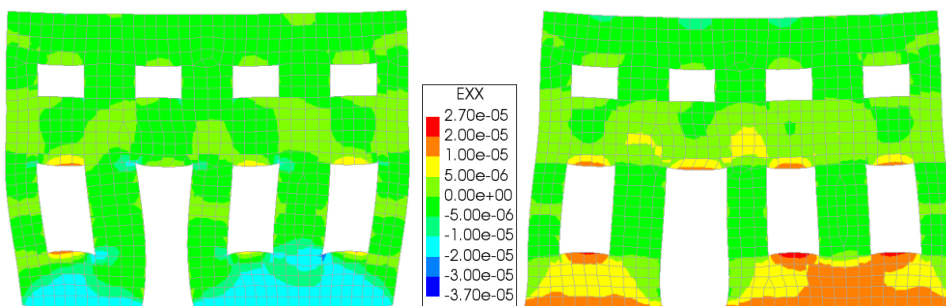


Figure 36. Horizontal strain façade C when subjected to *sagging* (left) and *hogging* (right). Deformed mesh magnified x5000.

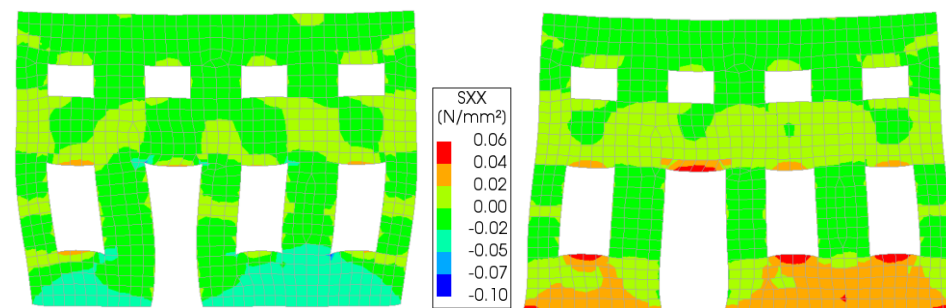


Figure 37. Horizontal stress façade C when subjected to *sagging* (left) and *hogging* (right). Deformed mesh magnified x5000.

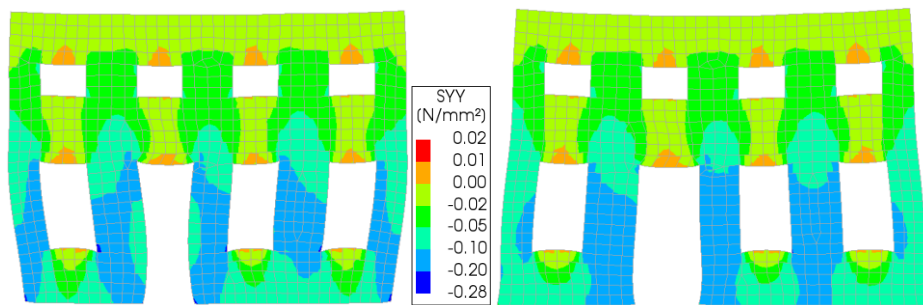


Figure 38. Vertical stress façade C when subjected to *sagging* (left) and *hogging* (right). Deformed mesh magnified x5000.

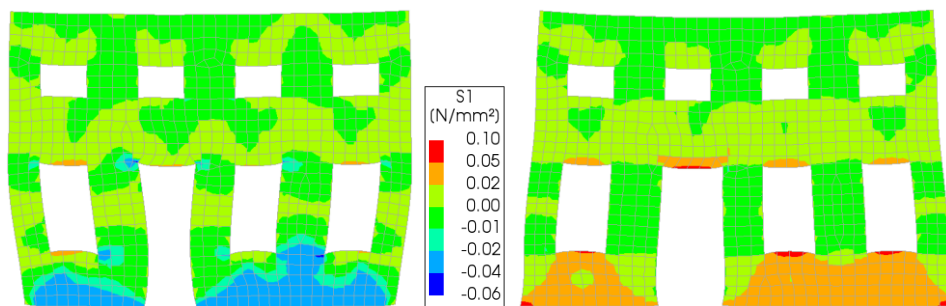


Figure 39. Principal stress façade C when subjected to *sagging* (left) and *hogging* (right). Deformed mesh magnified x5000.

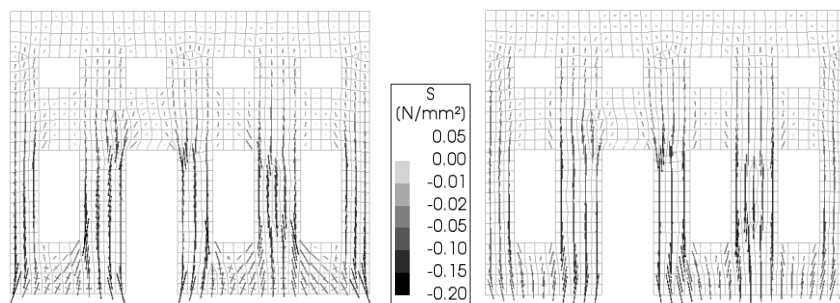


Figure 40. Principal stress compressive tensors façade C when subjected to *sagging* (left) and *hogging* (right). No deformed mesh.

3.2.3 Amplified Results

In order to evaluate the onset of visible cracking in the façade, the different displacement cases are again iteratively scaled up to the “visible damage” state complying with $\Psi_i = 1$, as described before for facades A and B.

Typical crack patterns detected in the façade when subjected to displacement amplification, are depicted in Figure 41. The figures shows the principal crack width for sagging and hogging. For sagging, cracks are mainly localized at the pier at the left side of the door. For hogging, cracks due to delamination at the two base corners of the façade and in the lintel above the door are present.

Additional sensitivity analyses for façade C are again investigated in the appendix.

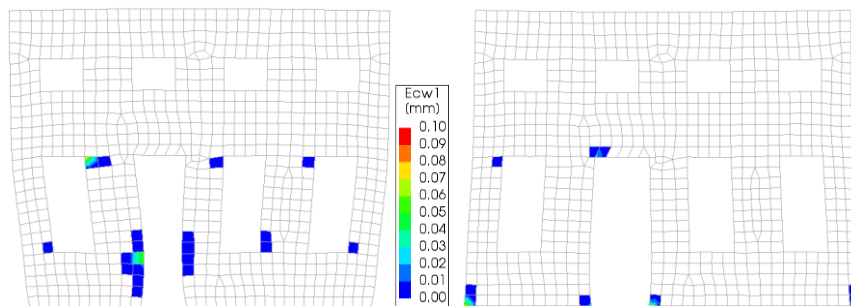


Figure 41. Principal crack width façade C. Maximum horizontal displacement applied as 50% of the original, and amplified 12.5 times (about 0.71 mm) for *sagging* (left), and 7.0 times (about 0.39 mm) for *hogging* (right). Deformed mesh magnified x500.

3.3 Sensitivity Study – Reduced Strain Transfer

The presented results can be considered as the worst case scenario since the horizontal strain of the soil is assumed to be fully transmitted to the façade's foundation, which is a conservative assumption. In this way, due to a direct pushing and pulling of the foundation, stress concentration and extra damage could occur at foundation level. In this section, a sensitivity study is performed on the horizontal displacement amplitude applied at the base of the façades. Values equal to 75%, 50%, 25% and 0% of the original 100% horizontal displacement are employed and analysed **Error! Reference source not found.**. The vertical displacement is a gain applied too and kept constant and equal to the original value (100%) since this is not affected by slipping between the foundation and the soil. As for the original (100%) displacement, all these cases do not show any damage in the masonry façade; this is expected since an even smaller strain is transferred to the façade. A variation study regarding the true boundary condition is treated in Appendix B, where a soil-structure interface with gapping and frictional slip is employed and results analysed.

Note that this approach also produces the case where 0% of the horizontal displacement is maintained, yet the vertical displacement is always kept untouched at 100%. This would correspond to the case where façades are subjected only to the curvature of the soil without any horizontal strains.

The results of these variations are incorporated in the following section.

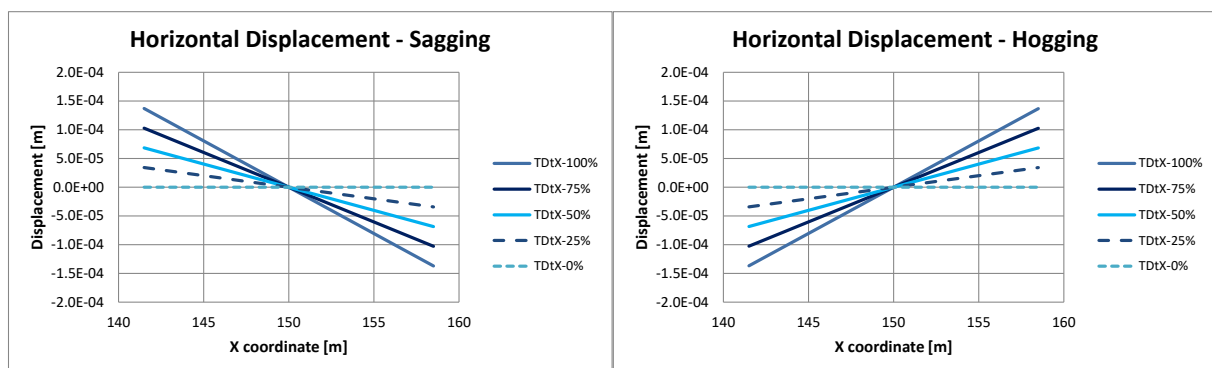


Figure 42. Variation of the horizontal displacements and thus horizontal strain applied to the base of the masonry façades A and B. Transmittal of horizontal strains is reduced to 75%, 50%, 25% and 0% of the original analysis with 100% transmittal.

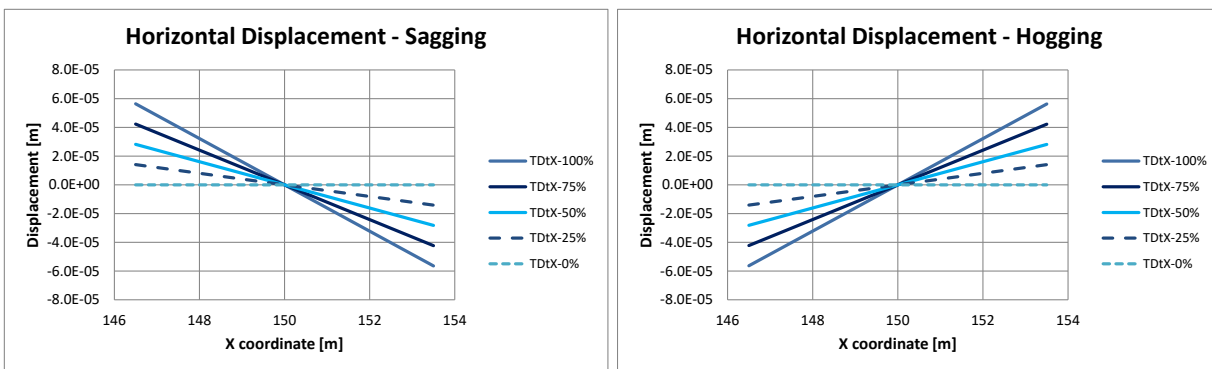


Figure 43. Variation of the horizontal displacements and thus horizontal strain applied to the base of the façade C. Transmittal of horizontal strains is reduced to 75%, 50%, 25% and 0% of the original analysis with 100% transmittal.

3.4 Summary of Results

An overview of the amplification factors, applied to the horizontal displacements of the different façades for sagging as well as hogging is tabulated in Table 1 and depicted with a plot in Figure 44. Figure 45 and Figure 46 show the direct comparison in terms of displacement amplification for the three different façade types and sagging/hogging cases. As can be seen, for façade A, the hogging settlement is almost twice as critical as the sagging one; façade A appears more vulnerable to this kind of displacement profile. Visible damage is reached when the original horizontal displacement is amplified about 11 times for sagging and 5.5 times for hogging, which corresponds to a maximum displacement of about 1.50 mm (strain of 17.6E-05) for the sagging and 0.75 mm (strain of 8.85E-05) for the hogging case. Façade C shows a similar trend, with amplification values close to façade A but slightly higher. The amplification for sagging is 12.5 against 10.85 for façade A and for hogging it is 7.0 against 5.5 for façade A. When the openings are increased in number and size (façade B), the margin or reserve for sagging increases. For this case, an amplification factor of 6.9 is necessary to reach a damage value of 1.0, which corresponds with a horizontal displacement of about 0.93 mm (strain of 10.9E-05). On the other hand, when subjected to hogging, the extra flexibility gained by the additional and larger openings, lets façade B appear slightly stronger than façade A (about 12% stronger). For all three façades, the hogging case remains the most vulnerable situation. Average values of horizontal displacement and horizontal strain which lead to visible damage ($\Psi_i = 1$) are listed in Table 2.

It is concluded that the margin (reserve) until the occurrence of a first visible crack varies between a factor 5.5 and 110 for the cases considered. The factor 5.5 corresponds to the worst case: 100% transmittal of horizontal strains, for hogging, and the long wall with small openings, positioned at the most unfavourable location in the settlement trough respectively heave trough. For the cases with 25% transmittal of horizontal strains (comparable with the realistic value of 30% from literature [5],[11][17]) the margin is a factor 16 to 39. Then considering the case of only horizontal strains with any vertical displacements (no curvature or angular rotation), the hogging values remain identical, while the margin for sagging increases slightly (11.2 vs 10.85 for façade A).

Finally, if a higher damage intensity is considered as the damage threshold with cracks of up to 1 mm in width, $\Psi_i=2$, as opposed to hairline cracks of 0.1 mm, $\Psi_i=1$, then the margin in respect to the existing soil deformation increases. However, for the hogging cases of the long façades (A and B), this increase is relatively small (only 27%) while for other cases it can reach up to 150% extra.

Table 1. Amplification factors of the different façades for different settlement profiles (sagging and hogging) and different horizontal displacement transmittal percentage, required to reach $\Psi_i = 1$.

Ψ_i	Displacement Percentage		Façade A		Façade B		Façade C	
	Horizontal	Vertical	Sagging	Hogging	Sagging	Hogging	Sagging	Hogging
$\Psi_i=1$	100%	100%	10.85	5.50	6.90	6.00	12.50	7.00
	75%	100%	14.80	7.30	9.00	8.00	16.00	8.50
	50%	100%	22.00	10.50	12.50	11.90	23.00	11.50
	25%	100%	39.00	16.00	21.20	19.00	36.00	17.50
	0%	100%	110.00	35.00	65.00	37.00	105.00	33.00
	100%	0%	11.20	5.50	7.60	6.00	13.10	7.00
$\Psi_i=2$	100%	100%	18.0	7.00	10.5	7.70	23.0	17.0

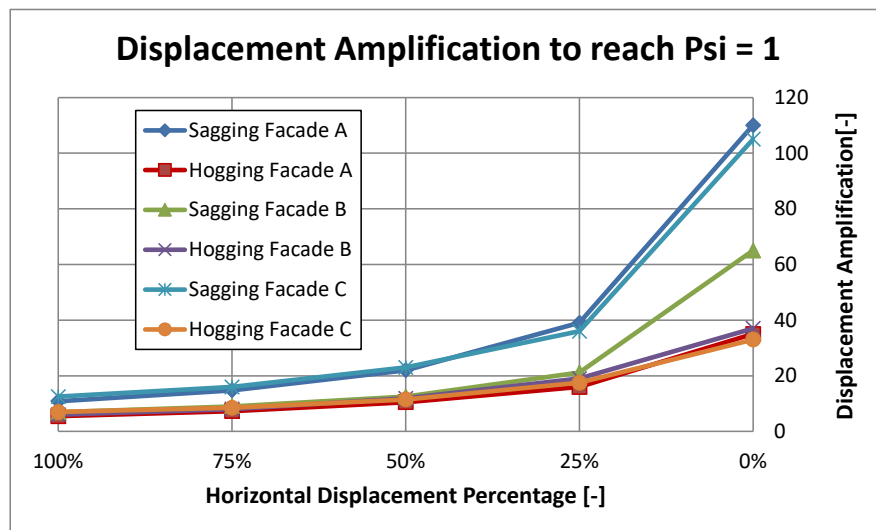


Figure 44. Horizontal displacement amplification for different settlement profiles and amplitudes required to reach $\Psi_i = 1$.

Table 2. Average horizontal displacement and strain of the different façades for different settlement profiles and amplitudes required to reach $\Psi_i = 1$.

Displacement Percentage	Applied	Sagging Facade A	Hogging Facade A	Sagging Facade B	Hogging Facade B	Sagging Facade C	Hogging Facade C
AVG Horizontal Displacement [mm]	0.14 FA-B 0.06 FC	1.50	0.75	0.93	0.82	0.70	0.40
AVG Horizontal Strain [-]	1.61E-05	17.6E-05	8.85E-05	10.9E-05	9.66E-05	19.5E-05	10.3E-05

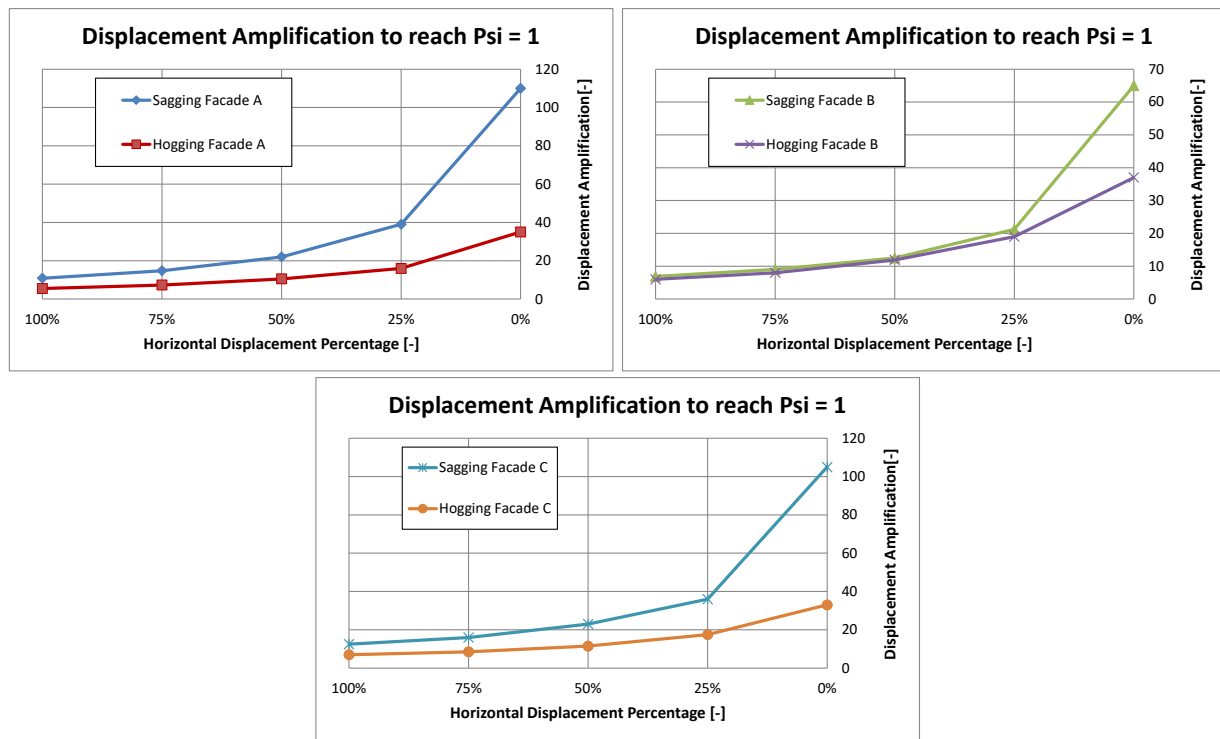


Figure 45. Horizontal displacement amplification for different settlement profiles and amplitudes required to reach $\Psi_i = 1$. Façade A (top left), façade B (top right) and façade C (bottom).

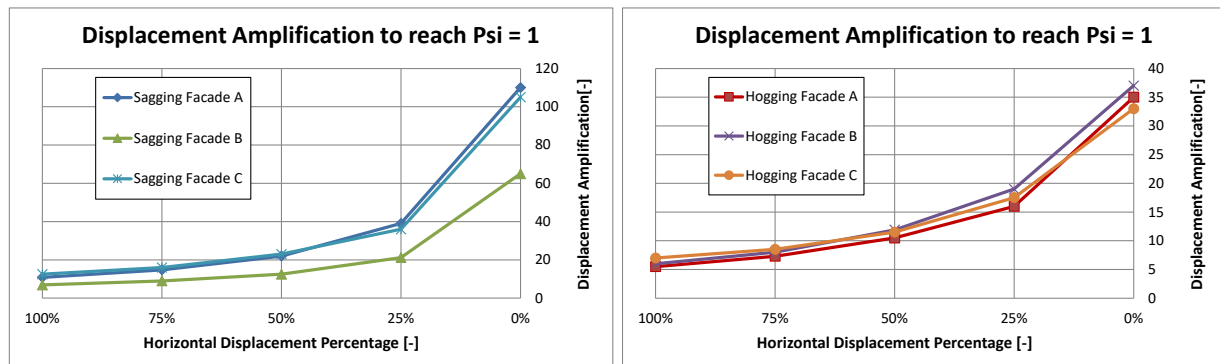


Figure 46. Horizontal displacement amplification for different façades and amplitudes required to reach $\Psi_i = 1$. Sagging (left) and hogging (right).

4. Discussion and Conclusions

The models presented herein have been developed as additional checks for worse-case scenarios where brittle masonry façades are subjected to horizontal and vertical displacements at the foundation. The study has been carried out on behalf of IMG, in a limited time frame. The mentioned displacements, expressed as horizontal strains and surface curvature, the latter also converted to angular distortion for various façade lengths, can be compared to those arising in Norg due to subsidence and heave, products of gas extraction and storage, respectively, to determine whether visible light damage can be expected. Summary Table 1 below carries out this comparison and will be dissected next.

Firstly, the geomechanical analytical model indicates a horizontal strain of 1.61E-5 for subsidence in the year of 1995, and a slightly lower strain for regular years, 1.14E-5 or 11.4 $\mu\text{m}/\text{m}$ (Table 1.a). For heave, the horizontal strains are smaller, in the order of 2.2 $\mu\text{m}/\text{m}$ (Table 1.b). These values are coupled to a small curvature of the soil which produces an angular distortion on the foundations of buildings. These existing values, even for the year of 1995, are smaller than the critical thresholds determined in this study (Table 1.c and 1.d). These thresholds are a combination of horizontal strain and angular distortion, which, if exceeded, would trigger visible damage in the masonry buildings.

Secondly, in comparison to results observed in literature from the consolidation literature study report [12], where the threshold for damage is given at 200 $\mu\text{m}/\text{m}$ of horizontal strain, 4.3E-4 rad of angular distortion or a combination thereof, the results of the finite-element models for sagging and hogging cases of the models where a realistic transfer of the horizontal strains is considered between soil and foundation (Table 1.e and 1.f) are well comparable. However, the more conservative approach, where 100% of the strains are transferred to the foundation, leads to lower critical values (Table 1.c). Furthermore, the results from the models can be viewed in an even more pessimistic manner and contemplate a façade with poor masonry, which leads to light damage about 25% earlier (Appendix D), including also existing cracks at the worst possible locations, which reduces the critical threshold back by a further factor of 2 (Appendix F), and even consider cyclic effects of ten years of sagging and hogging, which, in the worst case, led to a reduction of an additional 20% (Appendix C); this is presented in Table 1.i for a more realistic, yet conservative, 50% transfer. In comparison to literature [12], these pessimistic values are much lower.

Yet, in comparison to the existing soil strains as reported by the analytical model [13] in Table 1.a, these worst-worst case values are still a factor of 3.5 larger for the case of sagging (Table 1.i) and, even though hogging effects seem to affect masonry structures more intensely (Table 1.j), hogging is apparently less prevalent in Norg (Table 1.b) and so, the margin for hogging is much higher (about 13).

When looking at angular distortion without horizontal strains (0% transfer in Table 1.g), the models reveal critical thresholds much higher than the existing values of distortion (about 100 times larger). Yet, in comparison to literature [12] the values are much lower. In this case, this difference is attributable to the conservative modelling strategy which uses decoupled models; a coupled approach, where the presence of the foundation flattens the soil, would render more realistic and comparable results. In addition, the models assume a full application of the distortion to the foundation; in reality, even in the decoupled models, gapping can occur between the soil and the foundation which limits the application of the angular distortion. This is partially explored in Appendix B.

In this regard, the models must be seen as very conservative, not only are they decoupled, but they also assume that the façades are located at the worst position in the subsidence or hogging trough where the strains and curvatures are the highest. In reality, very few structures will be located at this position. Moreover, even in the decoupled model which does not reduce the strains in the soil, the assumption of 100% transfer of strains to the foundation is conservative. Literature suggests a value of only 30% [5] and Appendix B, where a realistic non-linear interface is explored, suggests even lower transference values when strains are high enough to produce visible light damage. Furthermore, Appendix E was used to explore the effect of a stiffer concrete foundation which led, predictively, to even lower transference values. At 10% transfer, the margin for a pre-damaged façade of poor masonry exposed to cyclic effects is a factor of 12. With this margin, most

modern buildings with concrete strips foundation are thus not affected by existing deep-soil effects regardless of the type of masonry present on the superstructure.

In addition, the definition for the threshold of damage employed in the models is strict. When $\Psi_i=1$ is reached, visible damage is considered to have appeared. A $\Psi_i=1$ corresponds to one crack of at least 0.1 mm; these hairline cracks are difficult to see in painted walls and almost indiscernible in bare masonry walls. Many studies [12] refer to wider cracks. Cracks of about 1 mm in width correspond roughly to a Ψ_i value of 2; these cracks are easy to see in bare masonry walls but are still considered light damage. To reach a damage of $\Psi_i=2$, the soil deformations must be increased between 27% and 150%; see section 3.4.

Summary Table 1. Comparisons of critical threshold values for building damage. Assuming always the most vulnerable façade.

Note: the characters underneath are used to reference table columns in the text.

Parameter	Units	Existing		Critical Thresholds for Building Damage $\Psi_i=1$							
		Geomechanical analytical model for regular years [13]		From Table 2 (100% transfer)		At realistic 30% Transfer [5]		Only Horz. Strain OR Angular Distortion		Poor masonry + pre-damage + cyclic effects at 50% transfer	
		Subsidence	Heave	Sagging	Hogging	Sagging	Hogging	Sagging	Hogging	Sagging	Hogging
Horizontal Strain	$\mu\text{m/m}$	11.4	2.2	110	90	300	240	115	90	80	50
Angular Distortion	10^{-8} rad	8.6	1.6	102	83	273	218	750	450	75	45
		a	b	c	d	e	f	g	h	i	j

In sum, the results confirm that the direct deep subsidence at Norg does not give any visible damage to the masonry; a wide margin exists before the appearance of visible light damage ($\Psi_i=1$). Yet, in comparison to literature, the worst-case models offer lower threshold values associated with the conservative nature of the models. The results provide an extra underpinning of the choice for the lower bound criterion for damage as a result from deep subsidence/heave [12],[16]. As the settlement trough in the Groningen field is not affected by the cyclic nature of gas storage/extraction and gives only slightly larger curvatures and horizontal strains as compared with the gas storage at Norg yet these values still below the worst columns in Summary Table 1, this conclusion can be extended to also hold for the Groningen field.

5. References

- [1] Boonpichetvong M., Netzel H., Rots J.G. (2006). Numerical analyses of soil-foundation-building interaction due to tunneling. In: Proc. 5th Int. Conf. on Geotechnical Aspects of Underground Construction in Soft Ground. Taylor and Francis.
- [2] <https://www.cellenbeton.nl/fysiek.htm>
- [3] Diana User's Manual -- Release 10.4, 2020; <https://dianafea.com/manuals/d104/Diana.html>
- [4] Voortgangsoverleg IMG-TNO-TU Delft, 23 November 2020.
- [5] Farrell R., Mair R., Sciotti A., Pigorini A. (2014). Building response to tunnelling. Soils and Foundations 54(3): 269-279.
- [6] Giardina G. (2013). Modelling of settlement induced building damage. PhD Thesis, TU Delft, 277 pp.
- [7] Korswagen P.A., Meulman E., Longo M., Rots J.G. (2018). Crack initiation and propagation in unreinforced masonry structures subjected to repeated load and earthquake vibrations. In: Proc. Int. Masonry Society Conferences, 0(222279), pp. 595-609.
- [8] Korswagen P.A., Longo M., Meulman E., Rots J.G. (2019). Experimental and computational study of the influence of pre-damage patterns in unreinforced masonry crack propagation due to induced, repeated earthquakes. In: Proc. 13th North American Masonry Conference, June 2019.
- [9] Korswagen P.A., Longo M., Meulman E., Rots J.G. (2019). Crack initiation and propagation in unreinforced masonry specimens subjected to repeated in-plane loading during light damage. Bulletin of Earthquake Engineering 17(8), pp. 4651-4687, 2019.
- [10] Korswagen P.A. (2021). InSAR Analyses of surface vertical settlements – Norg. TU Delft Memo 20210201 v2, IMG Project.
- [11] Mair R.J. (2003). Research on tunnelling-induced ground movements and their effects on buildings – Lessons from the Jubilee Line extension. In: Building response to tunnelling: Case studies from construction of the Jubilee Line extension, Eds. Burland J.B., Standing J.R. and Jardine F.M. CIRIA SP199 and Thomas Telford, London, pp. 3-26.
- [12] Ozer I.E., Geurts C.P.W. (2021). Literature review: Effects of subsidence on masonry buildings. TNO Report R12073, IMG Project.
- [13] Pluymakers M.P.D., Roholl J.A. (2021). Effecten diepe bodemdaling en -stijging rondom de Norg gasopslag en het Groningen gasveld. TNO Report R12068, IMG Project.
- [14] Rots J.G., Messali F., Esposito R., Jafari S., Mariani V. (2016). Computational modelling of masonry with a view to Groningen induced seismicity. In: Proc. 10th Int. Conf. on Structural Analysis of Historical Constructions (SAHC), 13-15 September, Leuven, Belgium, pp. 227-238.
- [15] Schreppers, G.M.A., Garofano, A., Messali, F., Rots, J.G. (2017). DIANA Validation report for masonry modelling. DIANA FEA BV & TU Delft, DIANA Report 2016-DIANA-R043 and TU Delft Report CM-2016-17, 143 pp., 15 February 2017.
- [16] Staalduin P.C. Van, Terwel K.C., Rots J.G. (2018). Onderzoek naar de oorzaken van bouwkundige schade in Groningen – Methodologie en case studies ter duiding van de oorzaken. TU Delft rapport CM-2018-01, faculteit CiTG, in opdracht van Nationaal Coordinator Groningen. Hoofdrapport 219 pp., bijlagen 49 pp.
- [17] Viggiani G., Standing J.R. (2001). The treasury. In: Building response to tunnelling: Case studies from construction of the Jubilee Line extension, Vol. 2, Eds. Burland J.B., Standing J.R. and Jardine F.M. CIRIA SP199 and Thomas Telford, London, pp. 351-366.
- [18] <https://www.thinklink.com/scene/1040171602467094531>
- [19] <https://berkela.home.xs4all.nl/skelet/skelet%20fundering%20op%20staal.html>

Appendix A: Material Parameters

The material parameters used in the models are listed below.

A.1 Soil

Soil layer properties of the first 30 m are taken from field data, while the remaining properties are taken from literature. The soil is modelled as linearly elastically. Diana automatically computes the initial stress when the gravity load is applied. The properties of the upper 30 m layers are employed also in the Shallow Soil Model (tier 2), in addition to the Deep Soil Model (tier 3).

Table 3. Soil layer material properties employed in the model.

Layer	Soil Depth [m]	Mass Density [Kg/m ³]	Poisson's Ratio [-]	Young's Modulus Top-Bottom [MPa]	K0 [-]	Mesh size [mxm]
1 - Silty Sand	0-9	1700	0.30	44.2 - 143.2	0.50	5x5*
2 - Clay	9-18	1700	0.45	77.0 - 151.0	0.65	5x5*
3 - Silty Sand	18-30	2000	0.35	393.7	0.50	5x5*
4 - Sand	30-60	2200	0.30	700.7	0.50	10x10
5 - Sand	60-100	2200	0.30	1430.0	0.50	20x20
6 - Rock	100-500	2500	0.22	1525.0	0.00	40x40
7 - Rock	500-1000	2500	0.22	6100.0	0.00	50x50
8 - Rock	1000-1500	2500	0.22	13725.0	0.00	50x50
9 - Rock	1500-3000	2500	0.22	24400	0.00	50x50

* 1x1 m for Shallow Soil Model

A.2 Masonry

The Engineering Masonry Model [14, 15] is used as material model for foundation and façade. The masonry façade is modelled with a thickness of 210 mm. The masonry foundation is modelled with a thickness of 610 mm. The local y axis of the finite elements is aligned to the global Y axis in order to define the bed joint orientation. The local x axis of the finite elements is aligned to the in-plane direction of the elements (global X).

Table 4. Masonry material properties employed in the model.

Property	Unit	Value
Young's modulus vertical direction E_y	MPa	5000
Young's modulus horizontal direction E_x	MPa	2500
Shear modulus G_{xy}	MPa	2000
Bed joint tensile strength $f_{t,y}$	MPa	0.15
Minimum head-joint strength $f_{t,x}$	MPa	0.45
Fracture energy in tension $G_{t,I}$	N/mm	0.01
Angle between stepped crack and bed-joint α	rad	0.5
Compressive strength f_c	MPa	8.5
Fracture energy in compression G_c	N/mm	20
Factor to strain at compressive strength	-	3
Unloading factor	-	Secant
Friction angle ψ	rad	0.64
Cohesion c	MPa	0.30
Fracture energy in shear G_s	N/mm	0.1
OOP shear failure	-	No
Crack bandwidth specification	-	Rots
Mass Density	Kg/m ³	1980

- MASONRY TRANSVERSAL WALLS: Linear elastic isotropic material is assigned to the beam elements representing the transversal walls. Note that no mass density is assigned to these elements. The stiffness is taken as three times lower than the one of the masonry. The cross-section of the transversal wall is taken as 210x210 mm for the façade and as 210x610 mm for the foundation. The use of such elements has been validated in [8].

Table 5. Masonry transversal wall material properties employed in the model.

Property	Unit	Value
Young's modulus E	MPa	1666.67
Poisson's ratio u	-	0.15
Mass Density	Kg/m ³	-

Appendix B: Sensitivity study – Soil-structure interface

B.1 Introduction

In the façade model presented in the report, the input displacements, which simulate the soil sagging/hogging deformation and the soil axial strains, are directly applied to the foundation of the façade (uncoupled analysis). At this location, such displacements, especially when amplified, can cause localization of stresses and could even cause some damage at the base of the façade. Furthermore, such full transfer of vertical and horizontal displacements from the soft soil to the stiff building is considered unrealistic; see also the summary and main report, and [5],[11][17]. An alternative modelling approach is to include a nonlinear interface between the structure and soil below the foundation, e.g. [1],[6]. In this appendix, a non-linear line interface with Coulomb friction for shear and gapping for tension is applied at the bottom of the structure (Figure 47). The goal is to observe whether the inclusion of this interface, which allows slipping and opening between the bottom of the foundation and the soil and so better mimics real structures, will lead to a different damage behaviour of the masonry façades.

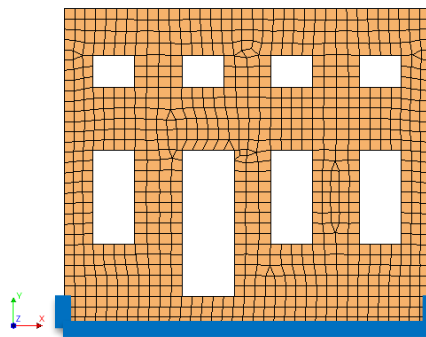


Figure 47. Non-linear interface applied at the bottom of Façade C.

B.2 Method

The interface is given a relatively high stiffness in the normal direction and a relatively low stiffness in the tangential direction (100 times lower than the stiffness in normal direction). The normal stiffness modulus is calculated from the formula $100 * E_{\text{masonry}} / \text{Meshsize}$. The interface is linear in compression, and follows the Coulomb friction criterion for shear behaviour. No tensile resistance is set to the interface, so no tensile forces can be transferred between soil and foundation. The properties used for the interface are shown in Table 6. All other model properties are kept equal to the main model presented in the body of this report.

Table 6. Non-linear interface material properties employed in the model.

Property	Unit	Value
Normal stiffness modulus k_n	N/mm ³	2500
Shear stiffness modulus k_t	N/mm ³	25
Cohesion c	MPa	0.002
Friction angle ϕ	rad	0.52
Dilatancy angle ψ	rad	0
Gapping Model - Tensile strength f_t	MPa	0
Model for gap appearance - Mode II shear	-	Brittle

B.3 Results

The results of façade C when subjected to sagging are shown in Figure 48, Figure 49 and Figure 50 in terms of contour plots of horizontal and vertical displacement and horizontal strain. The negative horizontal strain applied at the base (as the original values in Figure 4) produces the horizontal contraction at the base of the façade. The interface, which is conservatively applied also at the two lateral edges of the foundation assuming that the foundation is embedded in the soil, becomes fully compressed and transfers the full displacements to the façade; hence, the displacements of interface and façade are of similar values. The normal relative displacement plot of the interface when subjected to sagging is depicted in Figure 51. As can be seen, all points are under compression and thus transfer the entire displacement from the soil to the structure. Only a very small difference is found in the vertical component of the displacements. The change in the boundary conditions has thus only a small effect for sagging.

However, when hogging is applied, outward horizontal displacements are acting at the base of the façade. In this case, the interface gets pulled by the applied input displacements and the lateral side of it opens, transferring only a part of the displacement to the structure. This can be seen from the deformed mesh and displacement contour in Figure 52. The effect of the interface on vertical displacement and horizontal strain is shown in Figure 53 and Figure 54. Figure 55 shows the opening of the interface via the normal displacement at the end of the hogging load.

The amount of horizontal displacement that is transferred to the structure is plotted for the hogging situation against different displacement amplifications and for different façades (Figure 56). The plot tracks the ratio between the displacement of the bottom right corner of the façade and the displacement of the top node of the right lateral interface. The picture shows that the transferring of the displacement reduces when the load increases. This is equal to about 70-80% when the original input is applied and it drops to a plateau between 10 and 20% when the amplification factor increases to about 10. At this point, most of the displacement of the soil does not reach the façade as the bottom of the foundation slips over the soil.

In consequence, as can be seen from Figure 57 and Figure 58, no damage is found at the foundation level when this nonlinear interface is included (right pictures), since the stresses produced by the input actions are smeared out via the interface. The damage is much more localized in the façade and for the sagging case (Figure 57), the amplification factor to reach $\Psi_i=1.0$ is slightly lower than for the case without interface. For the hogging case (Figure 58), the damage occurs only for very high amplification factors of the displacement, since only a part of the input is transferred to the model. Table 7 lists the amplification factors to the displacement required to reach visible damage, i.e. a $\Psi_i = 1.0$. For sagging, the values are approximately the same for all three façades. For hogging the values to obtain visible damage are higher than for the case without interface, since the displacements are only partially transferred.

The case of the soil constraining the foundation at its sides for the sagging models is, however, a worst-case assumption. It is unlikely that the soil at the sides of a building will be capable of developing the passive pressure to enforce the compression strain required. In most cases, when the building is surrounded by soil, the soil will deform plastically instead of pushing the sides of the foundation. To quantify this effect, the interface is placed only at the bottom of the foundation, i.e. the short vertical lateral interfaces at the sides are omitted, the lateral compression achieved during sagging loading is therefore not active anymore. The horizontal displacement is now only transferred through the bottom edge. A comparison of horizontal displacements for this different case is plotted in Figure 59 and compared with the other cases. As can be seen, the displacements are partially transferred from soil to foundation due to plastic shear slip at the bottom interface and, high amplifications of the applied displacements do not cause damage to the façade. Further variations have also been made regarding the interface parameters (including k_n , k_t and friction angle) and these did not modify the main outcome.

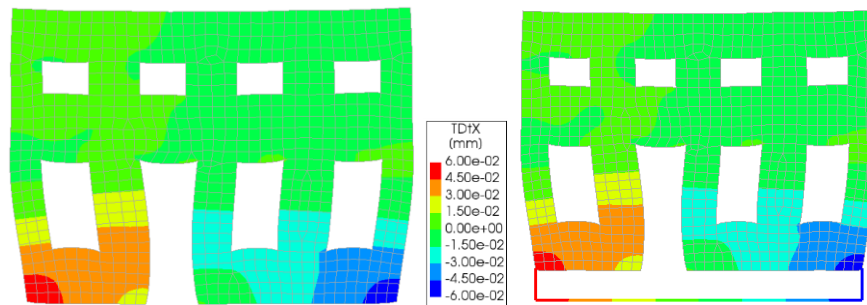


Figure 48. Horizontal displacement façade C when subjected to *sagging*. Model without interface (left) and with interface (right). Deformed mesh magnified x5000.

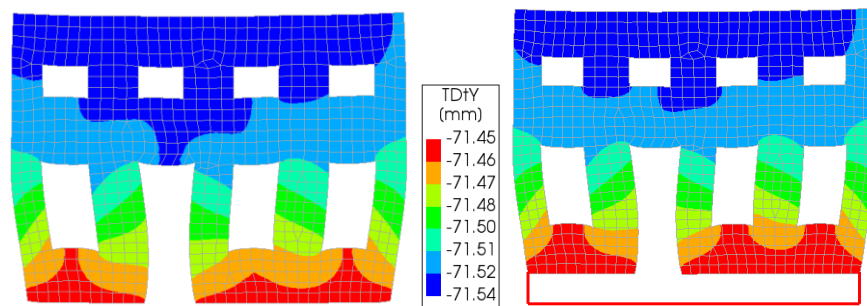


Figure 49. Vertical displacement façade C when subjected to *sagging*. Model without interface (left) and with interface (right). Deformed mesh magnified x5000.

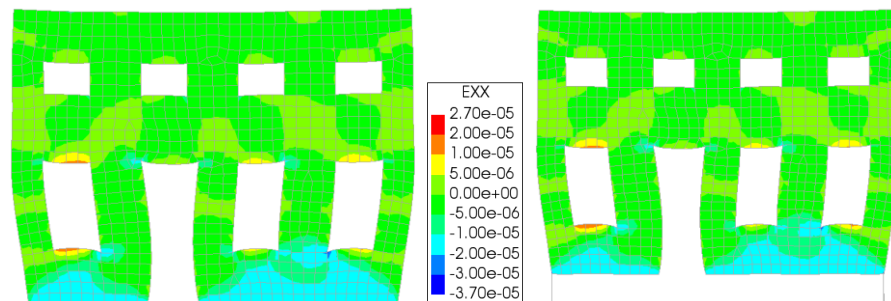


Figure 50. Horizontal strain façade C when subjected to *sagging*. Model without interface (left) and with interface (right). Deformed mesh magnified x5000.

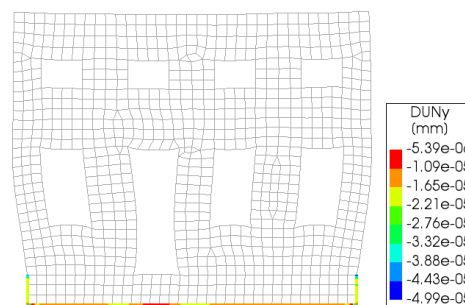


Figure 51. Interface normal relative displacement façade C when subjected to *sagging*. Deformed mesh magnified x5000.

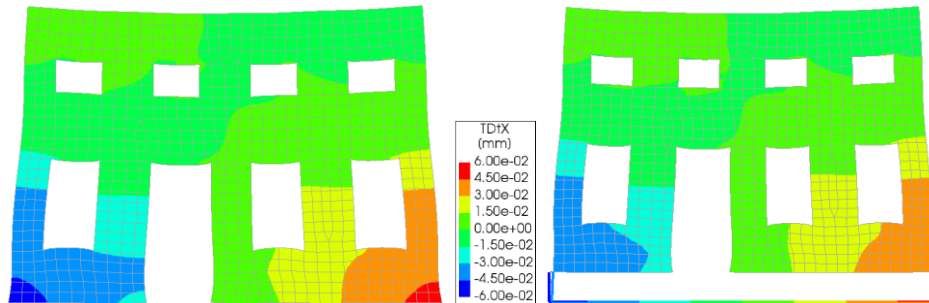


Figure 52. Horizontal displacement façade C when subjected to *hogging*. Model without interface (left) and with interface (right). Deformed mesh magnified x5000.

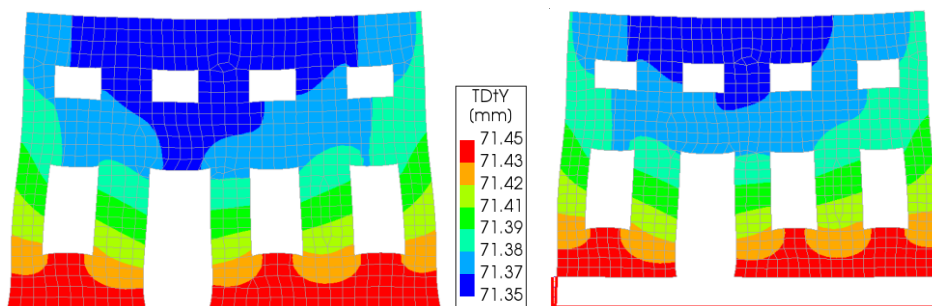


Figure 53. Vertical displacement façade C when subjected to *hogging*. Model without interface (left) and with interface (right). Deformed mesh magnified x5000.

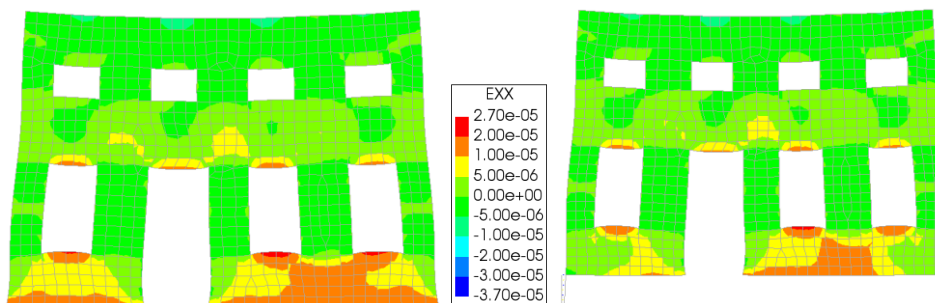


Figure 54. Horizontal strain façade C when subjected to *hogging*. Model without interface (left) and with interface (right). Deformed mesh magnified x5000.

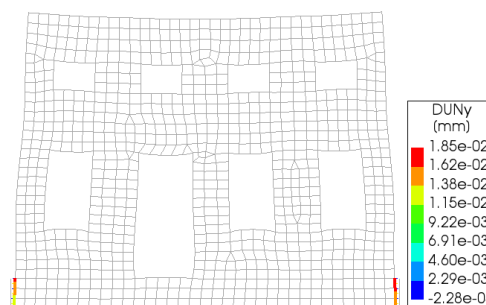


Figure 55. Interface normal relative displacement façade C when subjected to *hogging*. Deformed mesh magnified x5000.

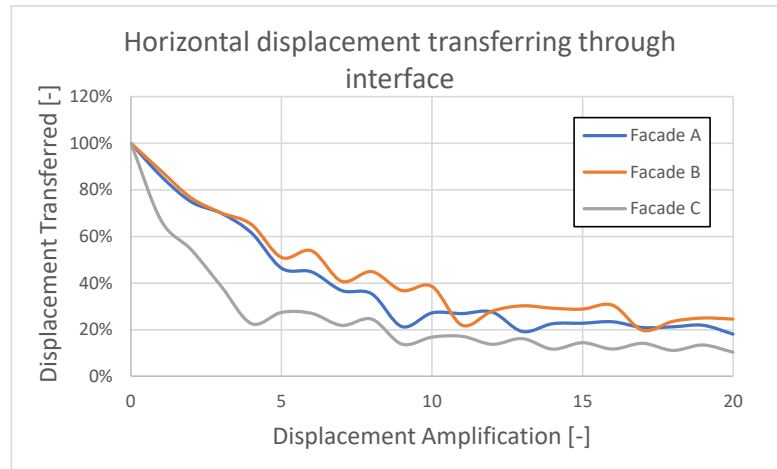


Figure 56. Evolution of the transfer of horizontal displacement from the soil via the interface to the façade, in *hogging* situation for increasing displacement amplification.

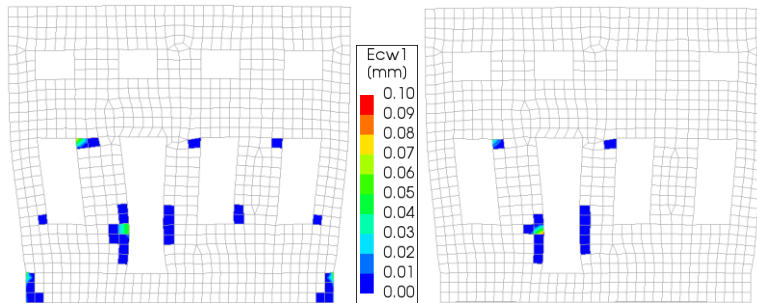


Figure 57. Principal crack width for façade C subjected to *sagging* displacements amplified by a factor 12.5 for the model without interface (left) and amplified by a factor 10.8 for the model with interface (right).

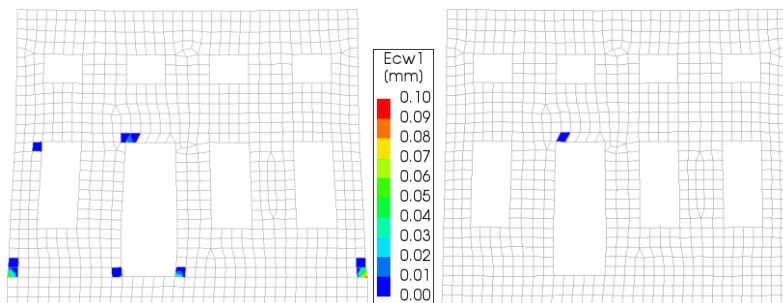


Figure 58. Principal crack width for façade C subjected to *hogging* displacements amplified by a factor 7.0 for the model without interface (left) and amplified by a factor 65 for the model with interface (right).

Table 7. Amplification factors of the applied soil displacements to reach $\Psi_i = 1$, for three different façades and the two different settlement profiles (*sagging* and *hogging*). The first row repeats the previous results of Table 1.

Case	Façade A		Façade B		Façade C	
	Sagging	Hogging	Sagging	Hogging	Sagging	Hogging
100% Without interface	10.85	5.50	6.90	6.00	12.50	7.00
100% With interface	10.85	32.00	7.30	32.00	10.80	67.00

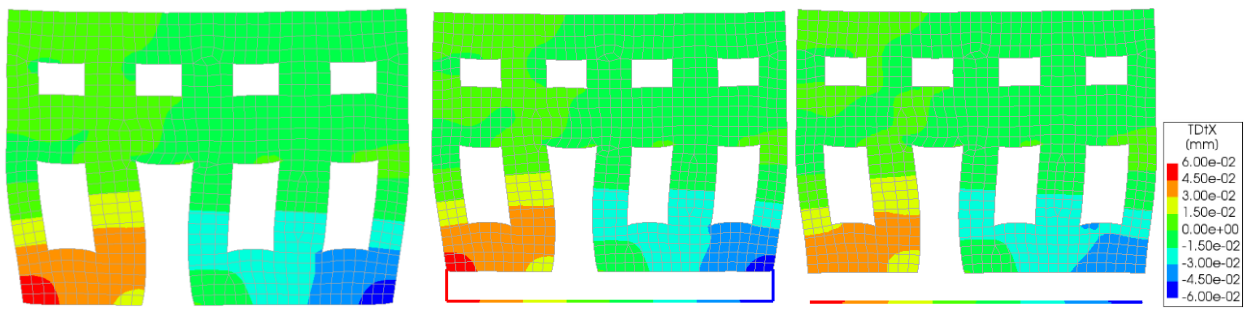


Figure 59. Horizontal displacement façade C when subjected to *sagging*. Model without interface (left), with full interface (middle) and only bottom interface (right). Deformed mesh magnified x5000.

B.4 Conclusions

As a variation to the fully uncoupled analyses in the main report, this appendix describes an additional study that checks the possible effect of the inclusion of frictional slip and gapping between building and soil. The conclusion is that for sagging the effect is very small when the sides of the foundation are also restricted as would be the case for neighbouring buildings. However, for hogging the margin/reserve up to the onset of visible damage increases about five times as compared to the uncoupled analysis without interface. This further verifies the fully uncoupled models are highly conservative.

Appendix C: Sensitivity study – Cyclic Loading

C.1 Introduction

An additional sensitivity study has been carried out in order to analyse the behaviour of the three façades when subjected to multiple sagging-hogging cycles as representative of the seasonal gas extraction (sagging) and gas injection (hogging) cycles of the Norg gas storage facility. The goal is to assess whether the repetition and cyclic nature of this loading type will trigger or lead to damage accumulation which would result in earlier damage onset or greater final damage.

C.2 Method

Two different loading protocols of 10 cycles are applied to the structures. The first loading protocol (Figure 60, left), is based on the sagging displacement amplified in such a way that visible damage of Ψ_i equal to 1.0 is obtained after the first monotonic branch simulating the sagging of the façade due to gas extraction. After that, the structure is displaced back to zero and then subjected to a gas-injection-induced hogging displacement with an amplitude of 50% that of the sagging amplification. This choice for a -1 down and +0.5 up scheme was inspired by field observations [10]. The second protocol instead (Figure 60, right) is based on the amplification factor to obtain visible damage ($\Psi_i = 1.0$) for the hogging displacement, while the sagging displacement is then amplified two times with respect to the hogging one. This complies with a +1 up and -2 down scheme, again inspired by field observations [10]. The amplification factors for the two cases and different façades are listed in Table 8. Since the amplification factors are dependent on the onset of damage, they vary for each façade. The bold amplification factors of Table 8 refer to the results of Table 9, which correspond to the monotonic amplification factor required to reach $\Psi_i=1$.

Table 8. Amplification factors of the three façades for the two different cyclic loading protocols. The values indicate the amplification factors for sagging and hogging (S-0-H-0) in the single cycle.

Load Protocol	Facade A	Facade B	Facade C
Sagging Based Cycles	10.85 - 0 - 5.43 - 0	6.90 - 0 - 3.45 - 0	12.50 - 0 - 6.25 - 0
Hogging Based Cycles	11.00 - 0 - 5.50 - 0	12.00 - 0 - 6.00 - 0	14.00 - 0 - 7.00 - 0

Table 9. Recap of amplification factors of the three façades for different settlement profiles and amplitudes required to reach $\Psi_i = 1$ when monotonic loading is applied. Taken from Table 1.

Displacement Percentage	Sagging Facade A	Hogging Facade A	Sagging Facade B	Hogging Facade B	Sagging Facade C	Hogging Facade C
100%	10.85	5.50	6.90	6.00	12.50	7.00

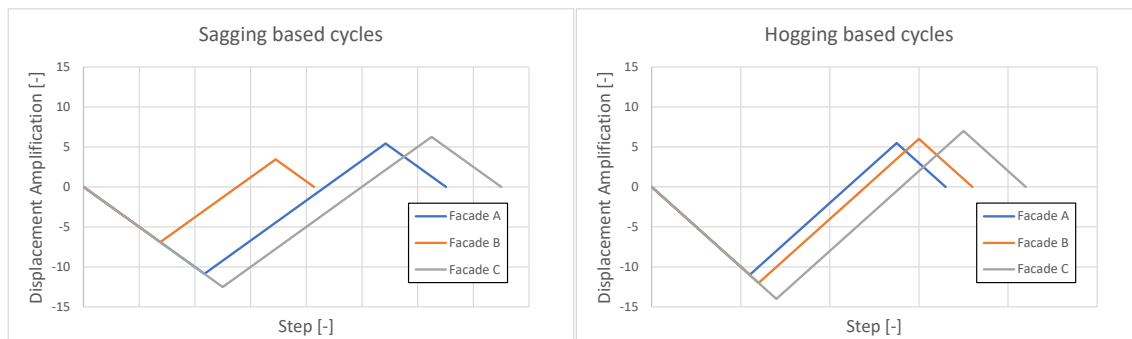


Figure 60. Single cycle based on sagging amplification factor (left) and hogging amplification factor.

C.3 Results

The maximum damage obtained during the 10-cycled protocol (cumulated damage) is extracted from the analyses. The results at the end of the first cycle and at the end of the protocol are depicted in Figure 61 to Figure 66. Results in terms of delta Psi (increment of damage) from the first to the tenth cycle, are tabulated in Table 10. As can be seen, façade A appears sensitive to the cyclic behaviour in both sagging and hogging based protocols. The repeated sagging and hogging displacement, which both have an amplitude close to the cracking point (according to Table 9), shows a “brittle” vertical type crack (of about 1 mm in width) below the window (Figure 61). Delamination cracks at the wall ends between wall and foundation also increase in width during the protocol. Similar behaviour is found in the hogging based cycles which have amplitudes similar to the sagging ones (Figure 62).

Façade B undergoes a different behaviour when subjected to cyclic loading with respect to façade A. During the sagging based cyclic protocol, the façade shows no increment in damage (Figure 63). In this particular protocol, the applied hogging amplification is 3.45, far from the factor 6.00 that would cause damage to a virgin structure. Consequently, the delta Psi (increment of damage) is equal to zero. When applying the hogging based cyclic protocol, the façade is subjected to a very high deformation while sagging. The damage state occurring in the structure then comes to a Psi equal to 2.5 (Figure 64). This can be interpreted as a “pre-damaged” façade. Yet, also in this case, the cyclic loading does not affect the increment of damage. Delta Psi is equal to zero after 10 steps. When the damage on the façade is caused by a single loading action (as only sagging or hogging), as can be the case of façade B subjected to sagging based loading, the cyclic loading is not influential to the final damage picture of the structure, i.e. Delta Psi is equal to zero.

Façade C reaches a damage value Psi = 1.0 upon amplifying the sagging displacement 12.5 times. The subsequent hogging displacement (amplified half of 12.5, thus 6.25 times) affects, in a light way, the damage of the façade. Delamination cracks between foundation and wall appear at the bottom corners of the façade, which increase the damage value to a Psi of 1.1 (Figure 65). The cycling protocol mainly influences the length and the width of such delamination cracks, bringing the final damage value up to Psi 1.4 (Delta Psi of 0.3). The heavier hogging based protocol shows an initial damage of Psi equal to 1.2 (Figure 66). The cyclic loading increases the damage value up to Psi 1.4 (delta Psi of 0.2).

An additional check is performed by combining the interface presented in Appendix B with the cyclic protocol. The hypothesis is that perhaps, the slipping interface, which allows sliding, will lead to accumulated damage in the façades. Or that the cyclic repetition will lead to a degradation of the interface. Consequently, the same protocol (starting with an amplification of 10.8 for sagging) is also applied to the same façade modelled with the friction/slip and gapping interface at the base as described in Appendix B. Opposite to the fully uncoupled analysis without interface (Figure 66), the hogging displacement has no influence on the structure (Figure 67). The reduction in stress provided by the interface when applying the input and the “softer” boundary have a positive effect on the cyclic behaviour; in fact, no increment of damage is found in such case.

Furthermore when the soil displacements and strains from the analytical geomechanics model [13] are cyclically applied in an un-amplified way, zero damage is detected for all the cases and no damage appears after the cyclic loading protocol. This is because the masonry remains linear-elastic (no cracking) and then cyclic loading has no effect at all compared to monotonic loading.

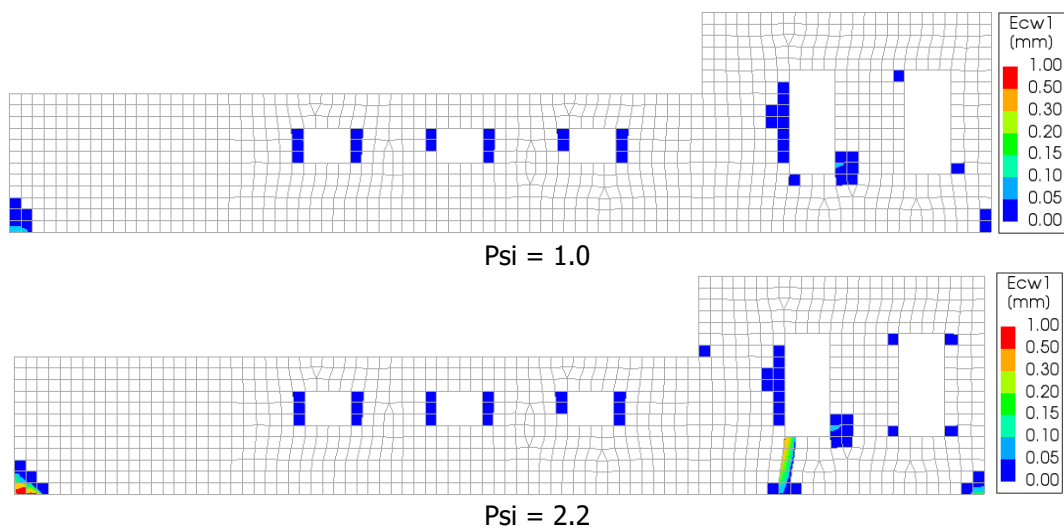


Figure 61. Maximum principal crack width Façade A with sagging based cycles. End of cycle 1 (top) and end of protocol cycle 10 (bottom).

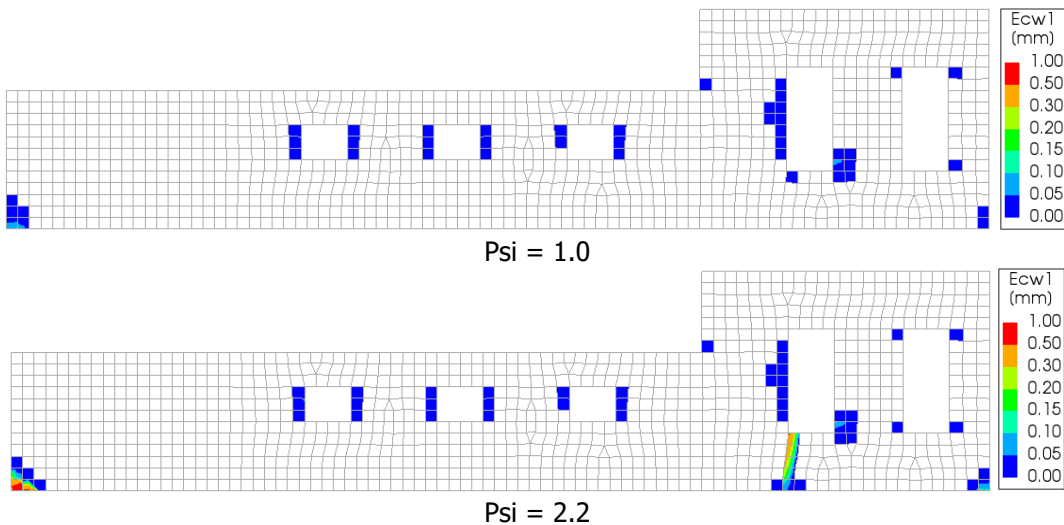


Figure 62. Maximum principal crack width Façade A with hogging based cycles. End of cycle 1 (top) and end of protocol cycle 10 (bottom).

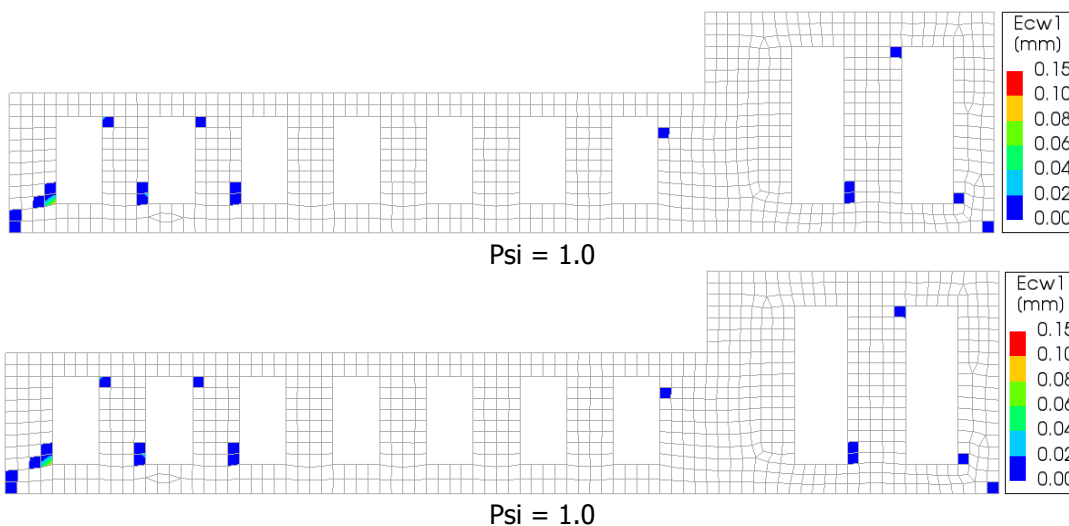


Figure 63. Maximum principal crack width Façade B with sagging based cycles. End of cycle 1 (top) and end of protocol cycle 10 (bottom).

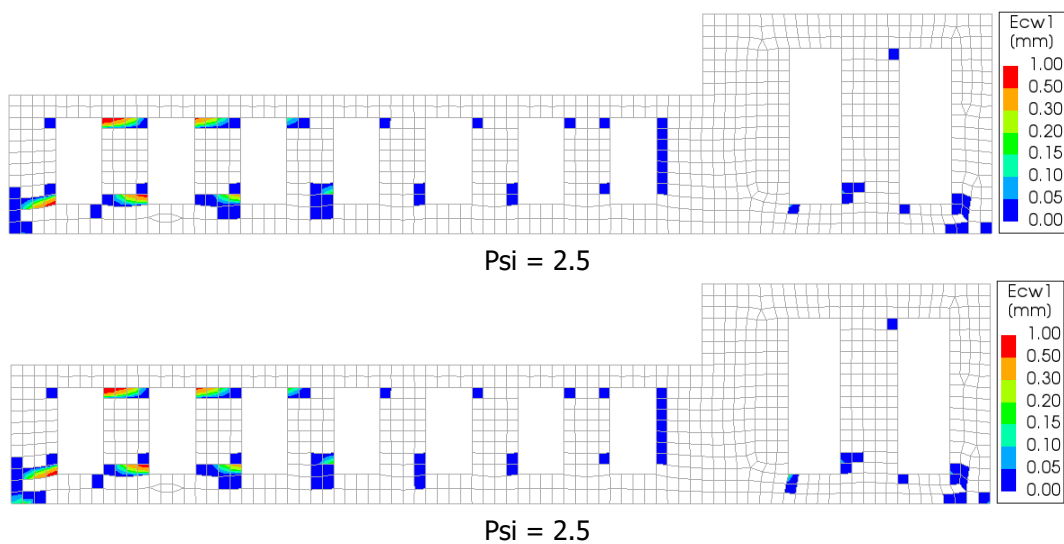


Figure 64. Maximum principal crack width Façade B with hogging based cycles. End of cycle 1 (top) and end of protocol cycle 10 (bottom).

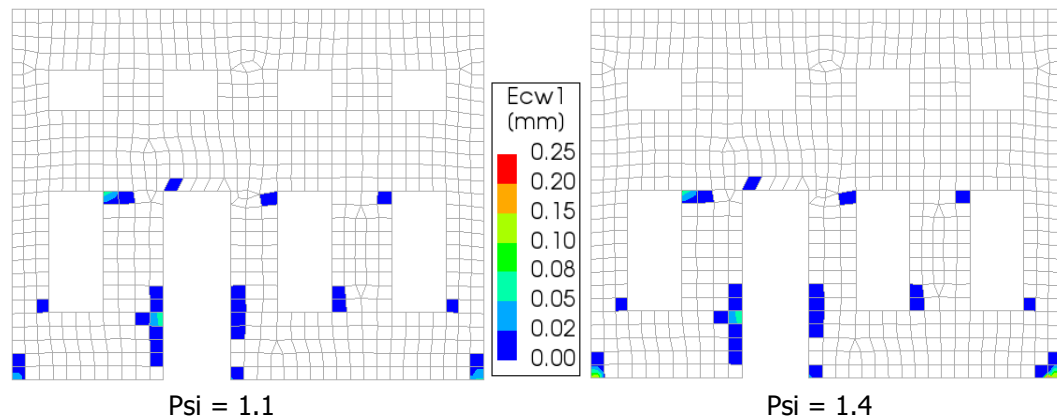


Figure 65. Maximum principal crack width Façade C with sagging based cycles. End of cycle 1 (left) and end of protocol cycle 10 (right).

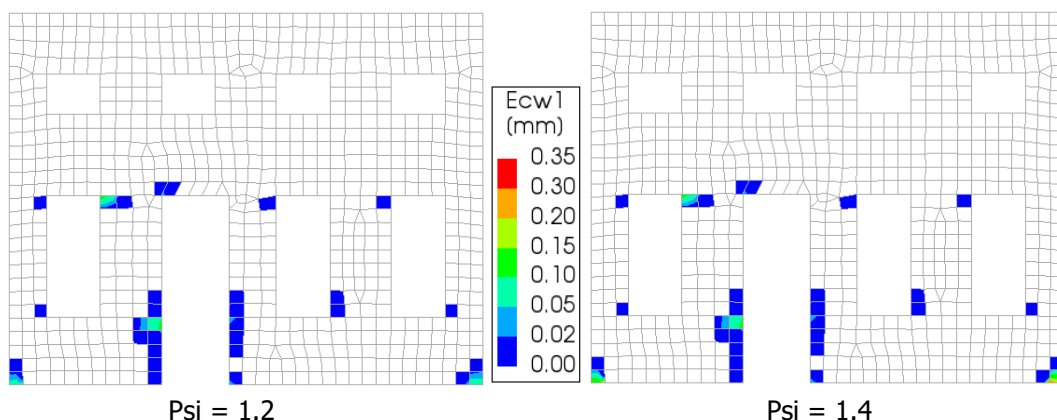


Figure 66. Maximum principal crack width Façade C with hogging based cycles. End of cycle 1 (left) and end of protocol cycle 10 (right).

Table 10. Increase in damage value ($\Delta \Psi_i$) between cycle 1 and cycle 10 of different façades for different cyclic loading protocols.

Load Protocol	Facade A	Facade B	Facade C
Sagging Based Cycles	1.2	0.0	0.2
Hogging Based Cycles	1.2	0.0	0.3

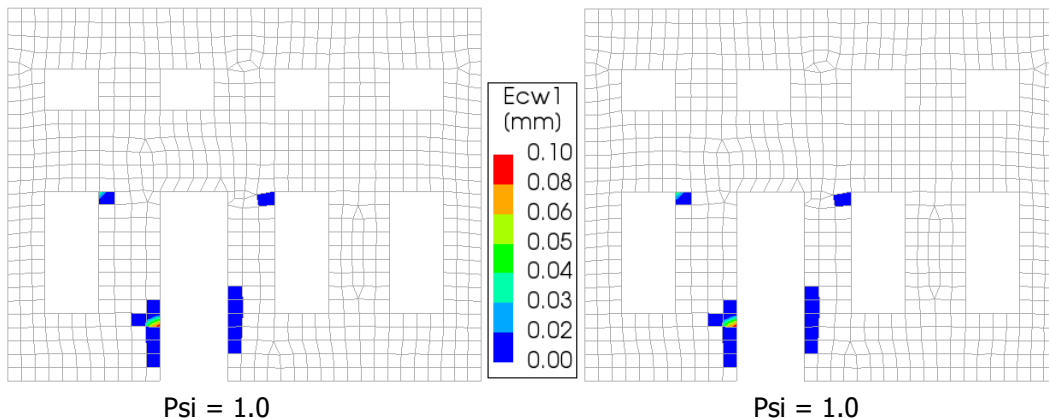


Figure 67. Maximum principal crack width Façade C with interface with sagging based cycles. End of cycle 1 (left) and end of protocol cycle 10 (right).

C.4 Conclusions

The analyses demonstrate that the cyclic models have the potential of predicting an increase of visible damage; this helps validate the models, indicating that they are capable of reflecting this damage increase when the boundaries and loading of the façades are sufficiently extreme.

Moreover, these analyses have shown that damage does increase when subjecting the façades to repeated sagging and hogging cycles. However, the façades are placed at the worst location and the soil displacements and strains estimated from the analytical model need to be amplified at least 5 times and be fully transferred to the structure before this extreme situation is reached. When no amplification is applied, that is, the horizontal strains and curvatures are those reported by the geomechanical analytical model [13], the masonry remains fully linear-elastic throughout the entire cyclic loading protocol and hence no damage nor damage accumulation is observed.

Hence, it can be concluded that the cyclic effect of seasonal gas extraction and storage can only lead to an accumulation of light damage if the displacements and strains due to deep-soil effects are much larger than currently present.

Appendix D: Sensitivity study – Masonry material properties

D.1 Introduction and Method

In order to provide a sensitivity study on the material properties of the façades, three additional materials (besides the original masonry material implemented in the main report) are investigated. The selected materials are:

- **Poor masonry:** it has the same elastic properties of the masonry, but with reduced tensile strength properties as compared to the masonry properties of Appendix A as employed in the main report. The bed- and head joint tensile strengths are reduced by 33.3% as well as the cohesion. The fracture energy in tension is reduced in order to obtain a softening branch which is parallel to the softening branch of the original material, thus preserving the same amount of "brittleness". This material can be seen as a poor, clay-brick type of masonry.
- **Aerated concrete masonry:** a different material is analysed. Cellenbeton G4/600 is selected. This material is in general less stiff than the above masonry, but it has comparable properties regarding tensile cracking behaviour. The shear behaviour is adapted to standard masonry formulations. The compressive strength is also reduced to 2.5 MPa. Material parameters are taken from [6]. Tensile strength properties are taken equal to the clay brick masonry properties, with adapted fracture energy so that the softening slope is the same as for the clay brick masonry. For the cohesion a value of 1.5 times the tensile strength in the bed joint is taken, as suggested in [14] The Young's modulus in vertical direction is taken from [2] and is equal to 2000 MPa, and the Horizontal Young's and shear modulus are selected by keeping the same ratio with the vertical one as in the above masonry material. The mass density is 600 Kg/m³.
- **Poor aerated concrete masonry:** as for the poor masonry, the tensile properties are reduced by 33.3%. The value of fracture energy, in this case, is selected such that the ultimate strain coincides with the ultimate strain of the standard aerated concrete masonry. Such material will have a slightly more ductile behaviour in tension with respect to the standard aerated concrete material.

Material properties are listed in Table 11. For the aerated concrete, the stiffness of the lateral beam elements representing the connection with the transversal walls is reduced proportionally to the material stiffness. The tensile behaviour of the four materials is shown in **Error! Reference source not found..**

The four materials are applied to the three façades. Both sagging and hogging deformation is investigated. The displacements applied at the base of the model (no interface is used) are amplified until the "light damage" boundary ($\Psi_i=1.0$) is reached.

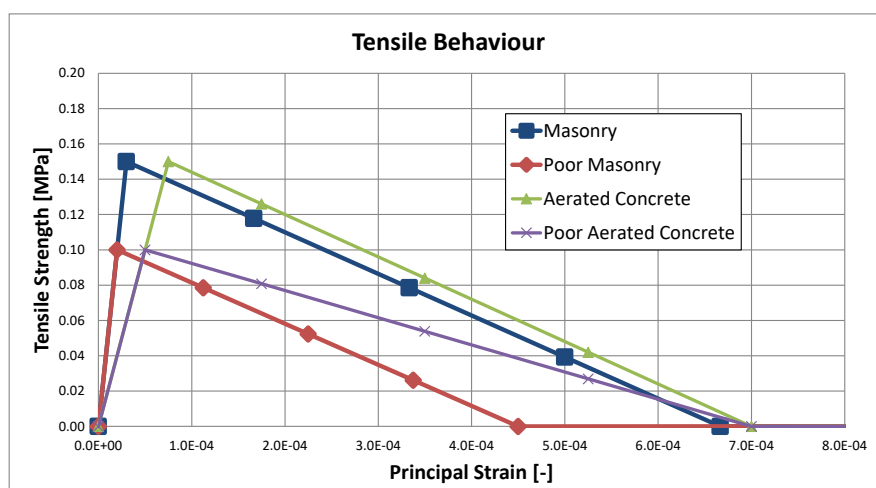


Figure 68. Tensile behavior selected materials.

Table 11. Variation of material properties.

Property	Unit	Material 1	Material 2	Material 3	Material 4
Material	[-]	Masonry	Poor Masonry	Aerated Concrete	Poor Aerated Concrete
Young's modulus vertical direction E_y	MPa	5000	5000	2000	2000
Young's modulus horizontal direction E_x	MPa	2500	2500	1000	1000
Shear modulus G_{xy}	MPa	2000	2000	800	800
Bed joint tensile strength $f_{t,y}$	MPa	0.15	0.10	0.15	0.10
Minimum head-joint strength $f_{t,x}$	MPa	0.45	0.30	0.45	0.30
Fracture energy in tension $G_{t,I}$	N/mm	0.0100	0.0045	0.0105	0.007
Angle between stepped crack and bed-joint α	rad	0.5	0.5	0.6	0.6
Compressive strength f_c	MPa	8.5	8.5	2.5	2.5
Fracture energy in compression G_c	N/mm	20	20	16.05	16.05
Factor to strain at compressive strength	-	3	3	3	3
Unloading factor	-	Secant	Secant	Secant	Secant
Friction angle ψ	rad	0.64	0.64	0.64	0.64
Cohesion c	MPa	0.300	0.200	0.225	0.150
Fracture energy in shear G_s	N/mm	0.1	0.1	0.1	0.1
OOP shear failure	-	No	No	No	No
Crack bandwidth specification	-	Rots	Rots	Rots	Rots
Mass Density	Kg/m ³	1980	1980	600	600

D.2 Results

The overview of the results is tabulated in Table 12. As can be seen from the results, the façades with Material 2 reach visible damage earlier than Material 1. The reduction is in a range from 13% to 20% for sagging and from 20% to 30% for hogging. The short façade (C) has a higher reduction for sagging, while the long façades (A and B) have a higher reduction for hogging. The crack locations are in general at the same as for Material 1. These effects are expected since the lower tensile strength and fracture energy reduces the global resistance of the structure without affecting the cracking pattern.

In contrast, the lower stiffness of Material 3, has a positive effect on all cases. In fact, for the same vertical and horizontal soil displacements (or strains), the structure is subjected to a lower stress. The façades are also able to better "follow the deformation provided by the soil movement", both for sagging and hogging. This is especially true for the long flexible façade B where the increase in amplification factor (required to reach $\Psi=1.0$) is 50% for sagging and 66% for hogging. Similarly, this behavior is also achieved when façades are modelled with Material 4. Here, it can be seen that the elastic properties are dominant with respect to the cracking properties. In fact, the amplification factors for the displacement input are still above the ones of Material 1 (values range from 10% to 40% higher). Accordingly, the reduction in material strength shows lower amplification factors with respect to Material 3. The slightly higher ductility (for tensile behavior) of Material 4 allows the façade to build up inelastic strain slower. This effect is shown in Table 13 which provides the difference in amplification factors between the material types with different tensile behavior. Material 2 is confronted with Material 1 and Material 4 is compared to Material 3. The (poor) aerated concrete displacement amplification are lower than the ones for clay brick masonry, which is investigated with a more brittle behaviour.

Table 12. Amplification factors for Materials 2, 3 and 4 and the relative difference with respect to Material 1 (in parenthesis), for the different façades for different settlement profiles and amplitudes required to reach Psi = 1. Comparison of models with different materials.

Case	Sagging Facade A	Hogging Facade A	Sagging Facade B	Hogging Facade B	Sagging Facade C	Hogging Facade C
100% Material 1	10.85	5.50	6.90	6.00	12.50	7.00
100% Material 2	9.40 (-13.4%)	3.70 (-32.7%)	5.50 (-20.3%)	4.10 (-31.7%)	10.00 (-20.0%)	5.70 (-18.6%)
100% Material 3	16.10 (+48.4%)	7.20 (+30.9%)	10.40 (+50.7%)	10.00 (+66.7%)	16.90 (+35.2%)	8.30 (+18.6%)
100% Material 4	14.10 (+30.0%)	6.00 (+9.1%)	8.90 (+29.0%)	8.40 (+40.0%)	13.70 (+9.6%)	7.50 (+7.1%)

Table 13. Relative difference in amplification factors of Material 2 versus 1, and of Material 4 versus 3, for the different façades for different settlement profiles and amplitudes required to reach Psi = 1. Comparison between poor and standard versions of the two materials.

Case	Sagging Facade A	Hogging Facade A	Sagging Facade B	Hogging Facade B	Sagging Facade C	Hogging Facade C
Material 2 vs Material 1	-13.4%	-32.7%	-20.3%	-31.7%	-20.0%	-18.6%
Material 4 vs Material 3	-12.4%	-16.7%	-14.4%	-16.0%	-18.9%	-9.6%

D.3 Conclusions

This appendix has studied sensitivities of the effect of masonry properties for clay brick masonry and aerated concrete masonry by analysing standard and poor versions of them. The margin/reserve for upscaling the displacements to a level corresponding to $\Psi_i = 1$ then varies from -33% up to +67% with respect to the base case of standard clay brick masonry with average properties, depending on the particular case (façade type and hogging or sagging displacements), all for the conservative assumption of 100% transfer of the horizontal soil strains to the foundation. The maximum decrease of 33% still results in a significant margin with respect to the actual displacements that occurred, recalling worst case assumptions of 100% transfer of horizontal strains, worst position of the facades at locations of maximum curvature and horizontal strain, and margin with respect to the most critical year of 1995 for the Norg soil movements.

Furthermore, the trends and observations gathered here can be extended to other materials with the notion that more flexible or more ductile materials than clay-brick masonry will present lower damage as long as their tensile strength is at least 0.1 MPa.

Appendix E: Sensitivity study – Foundation

E.1 Introduction

The North-East part of the Netherlands is characterized by relatively good soil in respect to the west side of the country. In fact, sandy soil at shallow depth is largely present in the Norg and Groningen area (Figure 69). Such type of soil allows for the use of shallow foundations, especially for low-rise buildings. In the past this method was also implemented on (sea) clay soil. In the Norg and Groningen area, a quite high percentage of buildings is thus built on shallow foundations (or “fundering op staal” in Dutch), about 85% (Figure 70).

The shallow foundations of masonry structures can be divided in different typologies: a masonry foundation, a concrete foundation or a concrete strip foundation (Figure 71). With the masonry foundation used in older structures and the strip foundations in newer structures.

The minimum depth for these foundations is 60 cm in order to avoid problems related to freezing. Based on the four types of foundations, a sensitivity study is performed to obtain more information about the role of the base regarding the damage to the superstructure when subjected to sagging and hogging. The masonry foundation is used in the main model, and it is the goal of this sensitivity study to evaluate whether the concrete foundations have a positive or negative effect on the development of light damage.

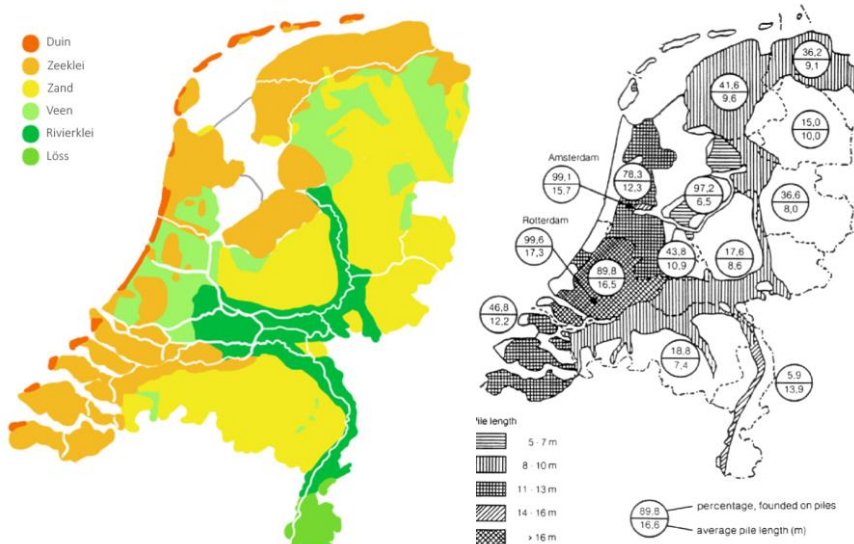


Figure 69. Left - Soil type Netherlands. [18]

Figure 70. Right - Percentage of structure founded on piles. Clearly shown: the high amount of shallow foundations in the North of the country.

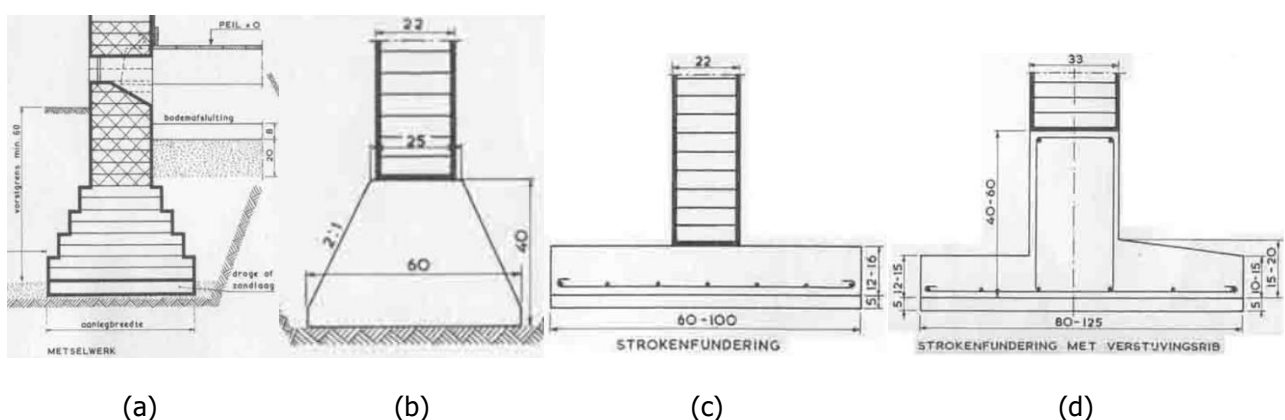


Figure 71. Shallow foundation typologies. Masonry foundation (a), concrete foundation (b) and strip foundations (c, d). [19]

E.2 Method

The modelling of the four different foundations is schematized in Figure 72. All dimensions are taken in a conservative way, so the minimum values reported in the drawings are selected. The first approach, called "Foundation 0" is the one already implemented in the main report. The other three shallow foundations have been modelled with different material and thickness in respect to Foundation 0. The reinforced concrete material is modelled as linear elastic. The properties are reported in Table 14. The results of the new three foundation types are compared to "Foundation 0" in terms of amplification displacement required to obtain a Psi value equal to one. The full comparison is made for the foundations implemented underneath Façade C with full (100%) horizontal and vertical sagging displacement applied to the foundation. Three different material properties are used for the masonry material, such as Material 1 (masonry), Material 2 (poor masonry) and Material 4 (poor aerated concrete) as defined in Appendix D.

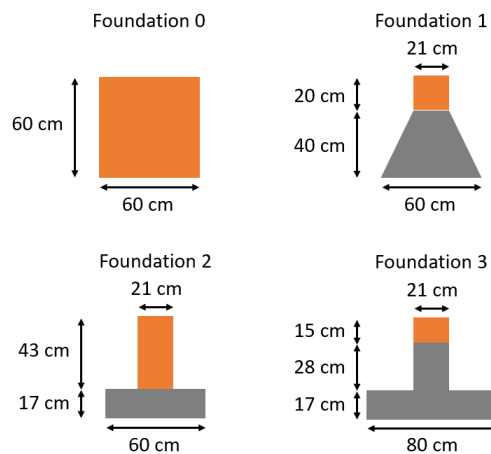


Figure 72. Schematization of different foundations. In orange at the top, masonry and in grey, concrete.

Table 14. Reinforced concrete material properties employed in the model.

Property	Unit	Value
Young's modulus E	MPa	31000
Poisson's ratio u	-	0.15
Mass Density	Kg/m ³	2500

E.3 Results

The results are listed in Table 15. As can be seen, the foundation modelled with non-linear masonry (Foundation 0) is still the most vulnerable. Comparing the concrete foundations, the effect of Foundation 3 results the most critical for the superstructure, with values comparable to the ones of Foundation 1. The extra stiffness provided at the base increases the stress localizations for both compressive and tensile forces (Figure 73). Such increase in stresses, though, remains concentrated at the foundation level and the effect on the superstructure are minimal. Damage patterns and crack location remain comparable between the two models. Foundation 3 appeared thus as the most critical foundation from the concrete ones and is therefore applied to the other two long façades (A and B) and analysed for both sagging and hogging displacement. Different material properties, namely Material 1, 2 and 4 are also investigated (see Appendix D). The results in terms of amplification factor when light damage occurs ($\Psi_i=1$) are tabulated in Table 16 and compared with the one of Foundation 0 (values in parenthesis). For all cases, the main masonry foundation (Foundation 0) is the most vulnerable. Similar values are obtained for the long façades, when hogging settlement is applied for both

masonry materials (1 and 2). The rest of the cases show an increment in amplitude factor of about 10-20% in respect to Foundation 0.

However, a stiffer concrete foundation may also modify the strain that is transferred to the superstructure if an interface between the soil and the foundation is included (see Appendix B). In order to compare the effect of such a foundation for what concerns the displacement transfer to the façade, a case with an interface representing the soil-structure interaction has also been analysed. The interface is modelled as described in Appendix B: Sensitivity study – Soil-structure interface and applied for the case of façade C with foundation type 3. The result in terms of horizontal displacement transfer percentage to the façade is depicted in the plot of Figure 74. The displacement transfer compares the horizontal displacement of the bottom right node of the façade to the top node of the lateral right interface. As can be seen from Figure 74, the stiffer concrete foundation reduces the amount of displacement transferred to the superstructure. In comparison to the traditional masonry foundation (F0), the more modern concrete foundation limits the transferred horizontal strain by an additional factor between 3 and 10.

Table 15. Amplification factors required to reach $\Psi_i = 1$ for Materials 1, 2 and 4 for façade C subjected to 100% sagging displacement. Comparison of models with different foundations.

Case	Foundation 0	Foundation 1	Foundation 2	Foundation 3
100% Sagging Material 1	12.5	14.0	15.5	13.8
100% Sagging Material 2	10.0	12.0	13.0	11.8
100% Sagging Material 4	13.7	15.8	21.0	15.6

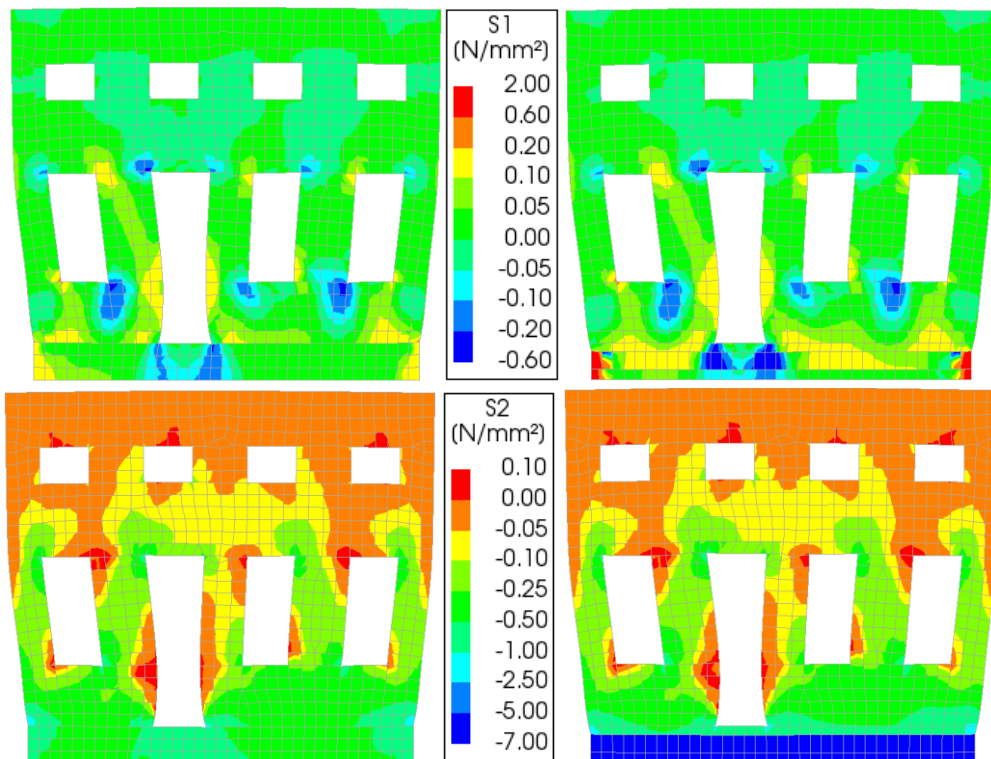


Figure 73. Principal stresses S1 (top), S2 (bottom) of Façade C subjected to 100% sagging at onset of cracking when modelled with Foundation 0 (left) and Foundation 3 (right). Amplification factors equal to 12.5 (left) and 13.8 (right).

Table 16. Amplification factors of the different façades for different settlement profiles (sagging and hogging) and different material properties, required to reach $\Psi_i = 1$. All cases are modelled with Foundation 3. In parenthesis values obtained with Foundation 0.

Material	Sagging Facade A	Hogging Facade A	Sagging Facade B	Hogging Facade B	Sagging Facade C	Hogging Facade C
Material 1 Masonry	12.20 (10.85)	5.50 (5.50)	8.10 (6.90)	6.10 (6.00)	13.80 (12.50)	8.00 (7.00)
Material 2 Poor Masonry	10.00 (9.40)	3.80 (3.70)	6.30 (5.50)	4.20 (4.10)	11.80 (10.00)	6.00 (5.70)
Material 4 Poor Aer Concrete	16.50 (14.10)	7.50 (6.00)	12.50 (8.90)	9.00 (8.40)	15.60 (13.70)	9.00 (7.50)

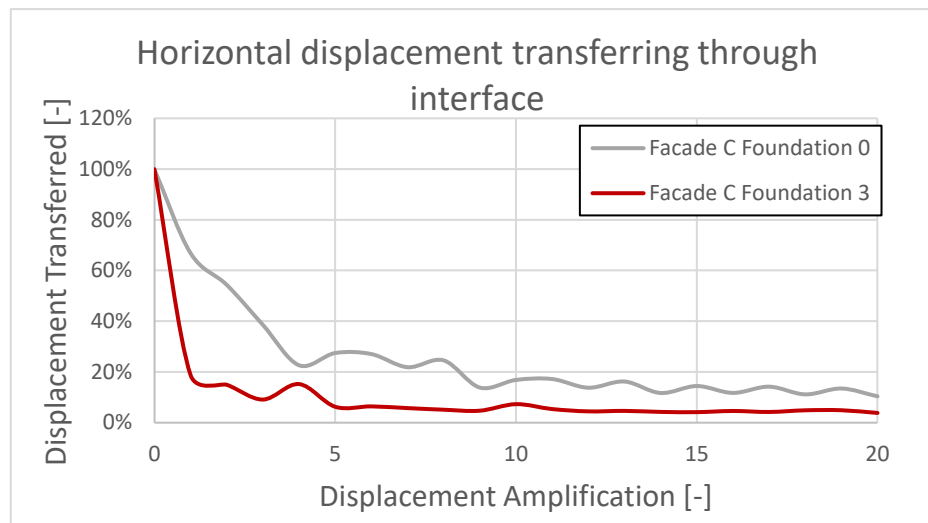


Figure 74. Evolution of the transfer of horizontal displacement from the soil via the interface to façade C, in hogging situation for increasing displacement amplification and different foundations.

E.4 Conclusions

Varying shallow foundation types have been modelled to observe the influence on the potential damage. A flat, strip concrete foundation (Foundation 3) was the most vulnerable but still led to overall higher amplifications factors than the traditional masonry foundation (Foundation 0) when the soil displacements were fully applied to the bottom of the foundation. However, when an interface between the soil and foundation was included, the stiffer concrete foundation helped reduce the strains transferred to the superstructure and led thus to significantly higher amplification factors (less damage) when compared to the masonry foundation with interface.

Appendix F: Sensitivity study – Pre-Damage

F.1 Introduction

Masonry buildings in the North area of the Netherlands and especially old constructions present different type of existing damage due to various causes such as uneven local settlements, cracks related to seasonal temperature and humidity phenomena or cracks related to vibrations from everyday use, traffic, nearby construction activities or earthquakes. In this Appendix the effect of existing damage (or pre-damage) in the façades is investigated. The objective is to gauge whether the pre-damage weakens the façades in a way that they become vulnerable to the effect of deep-soil actions presented herein as vertical and horizontal displacements at the bottom of the foundations.

F.2 Method

There are several methods in which pre-damage can be included in a model: the model can be subjected to an action that causes damage and then further subjected to the deep-soil displacements or the damage can be manually input in the model. The disadvantage with the first approach is that the damaging actions need to be precisely defined, while in the second method, the damaging actions are irrelevant and only the type of pre-damage is important. For the latter, engineering judgment of what kind of damage is observed is, however, required. In this appendix, the second method is employed and the pre-damage characteristics are assumed, in a manner consistent throughout this study, to be unfavourable.

This modelling approach has already been implemented in previous computational *and experimental* studies [8]. The pre-damage is included at various locations in the façade by weakening specific model elements by assigning a zero-tension material. This material is based on the properties of the virgin masonry material but includes a few modifications such as: halved elastic properties, no tensile strength (a value of 1E-5 MPa is used for numerical stability), reduced friction angle (1/3 of the original) and lower cohesion (10 times lower than the virgin case). No changes are made to the compressive behaviour (except for the reduced Young's Modulus). The material properties employed in the model are listed in Table 17. This set of properties is reasoned to correspond to an existing crack which offers no tensile strength but might be capable of resisting some shear and compression if fully closed.

For the three façades, different pre-damaged locations are selected and weakened. The studied cases are depicted in Figure 75. The pre-damaged area is shown in red colour. The selection of these areas is correlated with the location where the largest principal tensile stresses, such as window corners and window banks (spandrel below a window opening) are expected. Moreover, these locations are also the most fragile to accumulate damage for the cases of sagging and hogging; especially for façade C, pre-damage type 2, the entire façade could be split in two and single crack would concentrate the entirety of the deformations.

Table 17. Virgin and Pre-damaged material.

Property	Unit	Virgin Masonry	Pre-Damaged Masonry
Young's modulus vertical direction E_y	MPa	5000	2500
Young's modulus horizontal direction E_x	MPa	2500	1250
Shear modulus G_{xy}	MPa	2000	1000
Bed joint tensile strength $f_{t,y}$	MPa	0.15	1e-5 (~0)
Minimum head-joint strength $f_{t,x}$	MPa	0.45	1e-5 (~0)
Fracture energy in tension $G_{t,I}$	N/mm	0.01	1e-5 (~0)
Angle between stepped crack and bed-joint α	rad	0.5	0.5
Compressive strength f_c	MPa	8.5	8.5
Fracture energy in compression G_c	N/mm	20	20
Factor to strain at compressive strength	-	3	3
Unloading factor	-	Secant	Secant
Friction angle ψ	rad	0.64	0.43
Cohesion c	MPa	0.30	0.03
Fracture energy in shear G_s	N/mm	0.10	0.01
OOP shear failure	-	No	No
Crack bandwidth specification	-	Rots	Rots
Mass Density	Kg/m ³	1980	1980

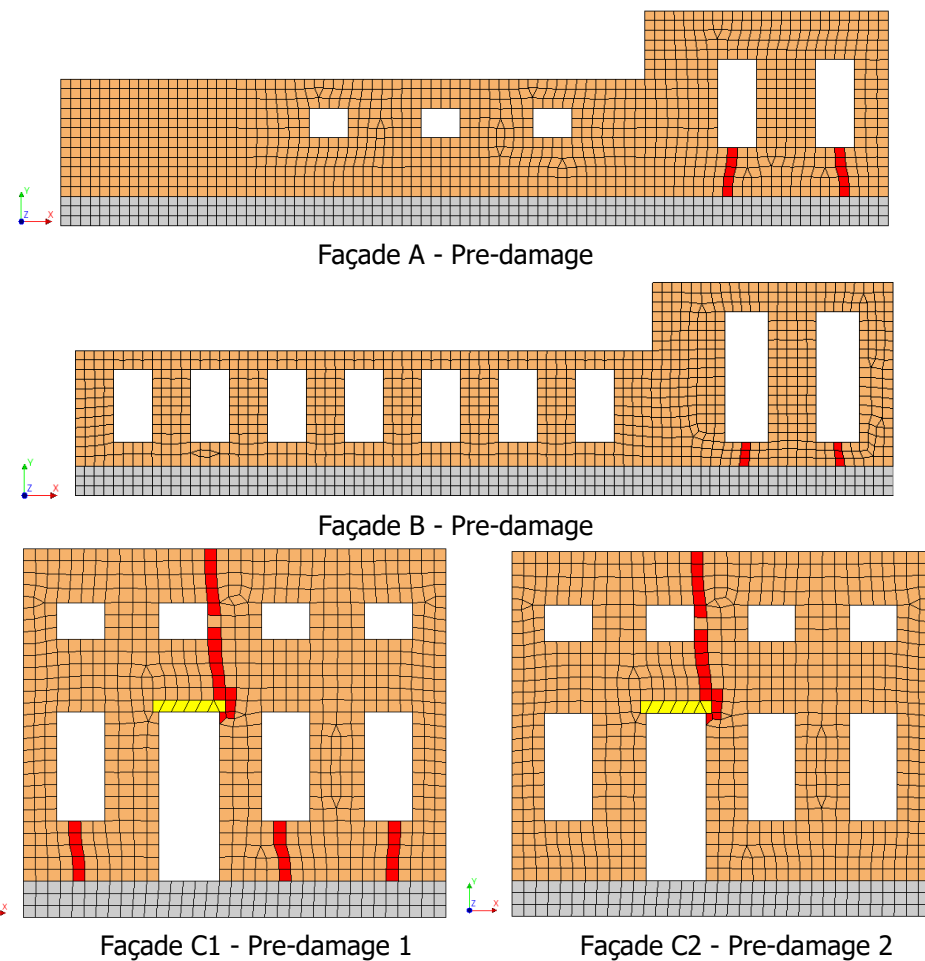


Figure 75. Pre-damaged cases for façade A (top), B (middle) and C (bottom). Pre-damaged area depicted in red.

F.3 Results

The results of the façades when subjected to monotonic hogging settlement are shown in Figure 76 and summarized in Table 18. The contour plots represent the principal crack width of the analyses when the displacements are amplified to reach a Ψ_i equal to 1; the table lists these amplification factors. As can be seen, some of the pre-damage cases, namely the one of façade A and C-1 reduce the displacement amplification factor to about half of its value. In such cases the location of the weak elements was prevailing in the change of the failure mechanism which mainly localizes at these weak spots. It must be noted that for the pre-damage cases, no initial Ψ_i is set (Ψ_{i0} equal to zero). This means that the tabulated final value is equal to the Delta Ψ_i ($\Psi_{iEnd} - \Psi_{i0}$), while in reality an initial damage should be already present (at least $\Psi_i=0.5$ corresponding to invisible damage). Yet, since this is not directly computable with this method of pre-damaging, the conservative approach of assuming an initial damage value of 0 is implemented. Including a correct initial damage value however, would scale up the amplification factor in the case that the final value refers to Delta Ψ_i equal to one. In other words, the computed value in this appendix refers to the most conservative cases.

As an additional comparison, the cases where the horizontal strains are transferred only at 25% (instead of 100%) are also evaluated. As with the 100% transfer models, the pre-damage has an important influence for façades A and C; the amplification factors are reduced by a factor of 1.7 in average, this is slightly smaller than the factor 2 for the 100% transfer cases which is advantageous.

Table 18. Amplification factors of the different façades for hogging settlement profiles and different pre-damage situation, required to reach $\Psi_i = 1$.

Transfer	Damage State	Hogging Facade A	Hogging Facade B	Hogging Facade C
100%	Virgin (Table 1)	5.50	6.00	7.00
	Pre-Damaged	2.75	6.00	3.50
	Pre-Damaged 2	-	-	7.00
25%	Virgin (Table 1)	16	19	17.5
	Pre-Damaged	8.8	19	11.4
	Pre-Damaged 2	-	-	17.5

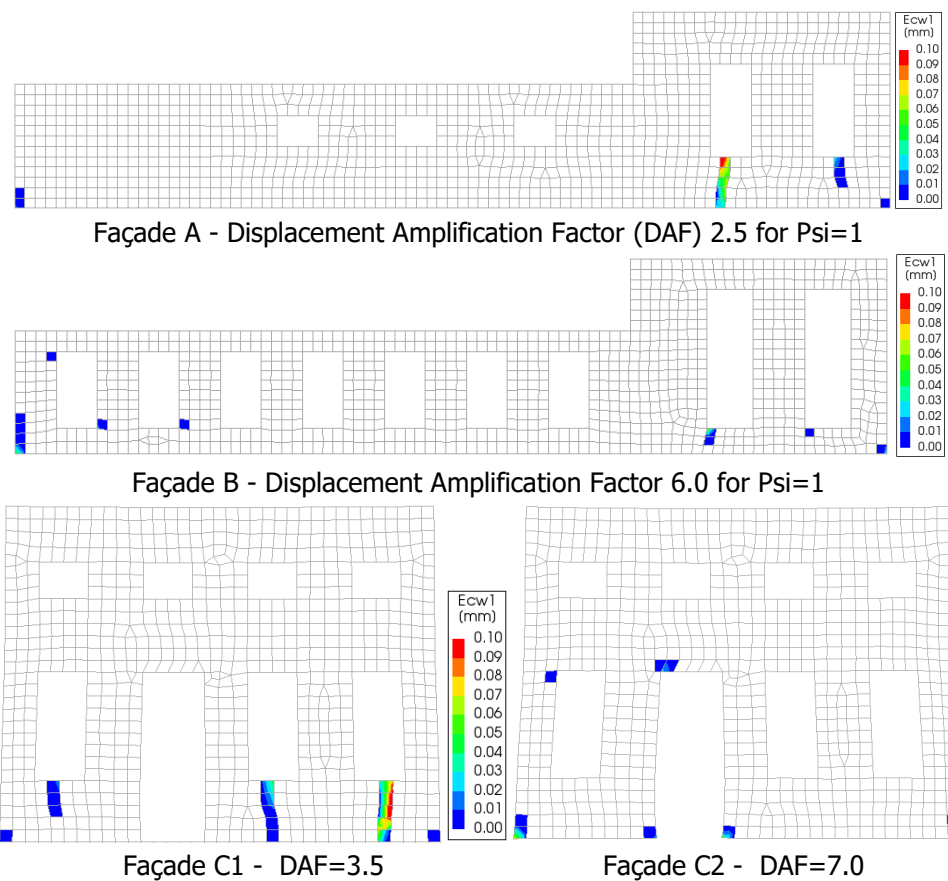


Figure 76. Principal crack width of pre-damaged cases when subjected to *hogging*, for façade A (top), B (middle) and C (bottom). Displacement amplified to reach the visible damage state.

In addition, for façade C, the loading protocol was also tested in cyclic behaviour. Two load histories are selected and compared to the "hogging based cycle" described in Appendix C. The loading protocols are shown in Table 19 and consist, for the virgin façade, of a sagging cycle with a DAF of 14, then 0, then hogging with DAF of 7 and then a return to zero; this is repeated ten times simulating ten years of gas extraction and storage. The damage pattern at the end of cycle 1 and end of the protocol for the different cases is shown in Figure 77 and Figure 78. The damage of the virgin case and the pre-damage case 2 are the equivalent to Figure 66 from Appendix C. This means that the cyclic effect does not aggravate the damage that occurs already after the first cycle.

Table 19. Amplification factors of façade C for the different cyclic loading protocols.
The values indicate the amplification factors for sagging and hogging (S-0-H-0) in a single cycle.

Load Protocol (LP) – Hogging Based Cycles	Sagging-0-Hogging-0
Façade C - Virgin	14.00 - 0 - 7.00 - 0
Façade C-1 LP1	7.00 - 0 - 3.50 - 0
Façade C-1 LP2	14.00 - 0 - 7.00 - 0
Façade C-2	14.00 - 0 - 7.00 - 0

Table 20. Psi values of façade C for the different cyclic loading protocols.

The values indicate Psi after the first cycle (S-0-H-0), the Psi at the end of the protocol (10x S-0-H-0) and in parenthesis the Delta Psi ($\Delta \Psi$) ($\Psi_{10} - \Psi_1$).

Load Protocol	$\Psi_{10} - \Psi_1$ (Delta Psi $\Delta \Psi$)
Façade C - Virgin	1.2 - 1.4 (0.2)
Façade C-1 LP1	1.4 - 1.4 (0.0)
Façade C-1 LP2	2.1 - 2.1 (0.0)
Façade C-2	1.2 - 1.4 (0.2)

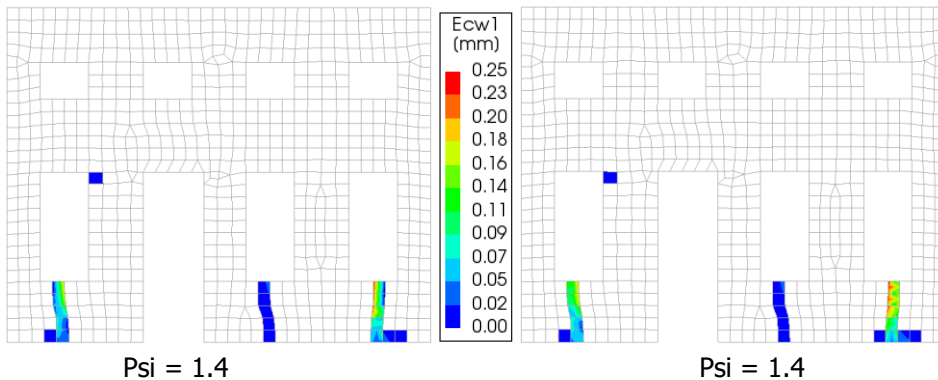


Figure 77. Maximum principal crack width Façade C with pre-damaged 1 and hogging based cycles PD1-1. End of cycle 1 (left) and end of protocol cycle 10 (right).

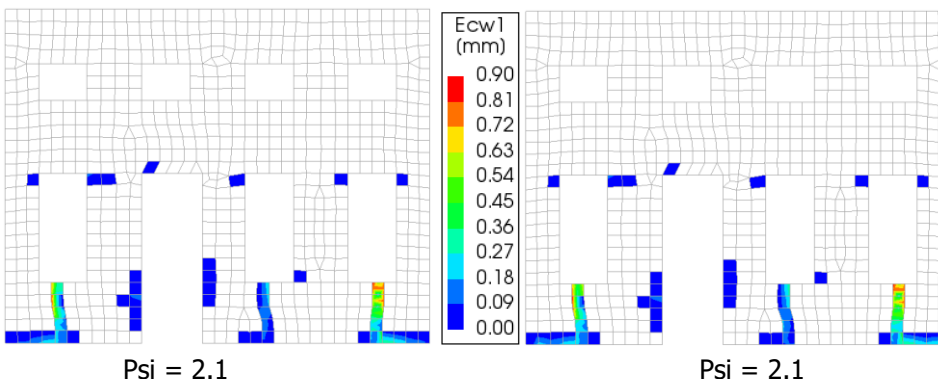


Figure 78. Maximum principal crack width Façade C with pre-damaged 1 and hogging based cycles PD1-2. End of cycle 1 (left) and end of protocol cycle 10 (right).

F.4 Conclusions

Existing cracks, positioned at unfavourable locations in the masonry façade, do reduce the margin between the values of strain and curvature determined by the geomechanical model and those required to cause visible damage in the masonry façades. This reduction is in the worst case a factor 2. Furthermore, a cyclic application of these displacements does not increase the final damage after ten cyclic applications in comparison to the first cycle. The pre-damage implemented represents open cracks not capable of withstanding any tensile stress and thus represent any visible crack regardless of its width. The reduction of a factor 2 and the cyclic application correspond to the full transfer of the soil displacements to the foundation. In case of 25% displacement transfer, the amplification factor increases to 8.8.